




Review

High Energy Density Welding of Ni-Based Superalloys: An Overview

Riccardo Donnini ^{1,*}, Alessandra Varone ², Alessandra Palombi ², Saveria Spiller ³, Paolo Ferro ^{3,*}
and Giuliano Angella ^{1,*}

¹ National Research Council of Italy (CNR), Institute of Condensed Matter Chemistry and Energy Technologies (ICMATE), Via R. Cozzi 53, 20125 Milan, Italy

² Department of Industrial Engineering, University of Rome Tor Vergata, Via del Politecnico 1, 00133 Rome, Italy; alessandra.varone@uniroma2.it (A.V.); alessandra.palombi@uniroma2.it (A.P.)

³ Department of Management and Engineering, University of Padua, Stradella S. Nicola 3, 36100 Vicenza, Italy; saveria.spiller@unipd.it

* Correspondence: riccardo.donnini@cnr.it (R.D.); paolo.ferro@unipd.it (P.F.); giuliano.angella@cnr.it (G.A.)

Abstract: High energy density technologies for welding processes provide opportune solutions to joint metal materials and repair components in several industrial applications. Their high-performance levels are related to the high penetration depth and welding speed achievable. Moreover, the localized thermal input helps in reducing distortion and residual stresses in the welds, minimizing the extension of the fusion zone and heat-affected zone. The use of these welding technologies can be decisive in the employment of sophisticated alloys such as Ni-based superalloys, which are notoriously excellent candidates for industrial components subjected to high temperatures and corrosive work conditions. Nonetheless, the peculiar crystallographic and chemical complexity of Ni-based superalloys (whether characterized by polycrystalline, directionally solidified, or single-crystal microstructure) leads to high susceptibility to welding processes and, in general, challenging issues related to the microstructural features of the welded joints. The present review highlights the advantages and drawbacks of high energy density (Laser Beam and Electron Beam) welding techniques applied to Ni-based superalloy. The effects of process parameters on cracking susceptibility have been analyzed to better understand the correlation between them and the microstructure-mechanical properties of the welds. The weldability of three different polycrystalline Ni superalloys, one solid solution-strengthened alloy, Inconel 625, and two precipitation-strengthened alloys, Nimonic 263 and Inconel 718, is reviewed in detail. In addition, a variant of the latter, the AF955 alloy, is also presented for its great potential in terms of weldability.

Keywords: Ni-based superalloy; microstructure; laser beam welding; electron beam welding



Academic Editors: João Pedro Oliveira and Zhi Zeng

Received: 28 November 2024

Revised: 20 December 2024

Accepted: 25 December 2024

Published: 1 January 2025

Citation: Donnini, R.; Varone, A.; Palombi, A.; Spiller, S.; Ferro, P.; Angella, G. High Energy Density Welding of Ni-Based Superalloys: An Overview. *Metals* **2025**, *15*, 30. <https://doi.org/10.3390/met15010030>

Copyright: © 2025 by the authors. Licensee MDPI, Basel, Switzerland. This article is an open access article distributed under the terms and conditions of the Creative Commons Attribution (CC BY) license (<https://creativecommons.org/licenses/by/4.0/>).

1. Introduction

Nickel-based superalloys are considered the most suitable alloys for mechanical components for which superior performance levels are required: they should resist high-temperature conditions that induce creep phenomena and exhibit excellent resistance to surface degradation (corrosion and oxidation). There is a wide range of possible applications for Ni-based superalloy components where temperature and operating conditions are particularly severe. The primary application for which these alloys were designed is gas turbines, to be employed both in power generation plants (e.g., thermo-electrical or nuclear

power plants) and in the aerospace industry as rockets and airplane engines [1]. Indeed, more than 40% of the total weight of modern aircraft is made of Ni-based superalloys [2]. In addition, superalloys are widely used in chemical and industrial plants, in the oil and gas industry, and for military vehicles and equipment [3].

In Ni-based superalloys, Ni is the main constituent, giving rise to austenitic FCC matrix γ . To provide high strength, several alloying elements, such as Cr, Ti, Al, Co, Fe in high concentrations, and Nb, Mo, W, and Ta in minor concentrations, are added to obtain solid solution and precipitation strengthening [4,5]. The solid solution strengthening mechanism is based on the distortion of the crystal lattice of the γ phase due to the presence of alloying elements characterized by different atomic radii. The distortion of the lattice hinders the dislocation movement, even forming Cottrell's atmospheres [6]. Moreover, depending on the local concentration of solute atoms, regions with altered elastic properties further restrain the deformation of the matrix [7]. The precipitation strengthening mechanism is mainly due to the precipitation of the γ' (Ni_3Al or Ni_3Ti) strengthening phase, which presents a L1_2 crystal structure and can precipitate in different shapes and sizes, misfitting the lattice parameters. Solid solution strengthening might also affect the γ' phase. Some alloys (e.g., Inconel 718, Inconel 625, and Inconel 706) present also the precipitation of the secondary phase γ'' (Ni_3Nb), with crystal structure D0_{22} [2]. γ' phase appears to be more thermally stable than the γ'' phase since γ'' phase transforms into δ phase at high temperatures [4,8–11]. δ phase indeed has a platelet morphology, is incoherent with the matrix, and does not contribute to its strengthening [8].

In this context, different microstructures with different crystalline grain configurations (polycrystalline, directionally solidified, or single crystalline) can be beneficial depending on the application. For example, polycrystalline superalloys are used in tube sheets, rods, and combustion chambers [12]. Polycrystalline alloys are indeed prone to grain boundary failure, which occurs because of corrosion, thermal fatigue, or creep induced by the high temperature coupled with mechanical stresses. In high-temperature applications such as gas turbine blades, these issues can be contrasted by inducing an oriented microstructure through directional solidification. This creates a microstructure composed of elongated columnar grains in the direction of maximum strain that extends the life span of a blade. More advanced and expensive processes allow the creation of single crystal alloys, in which the issue of the sliding grain boundaries is completely removed. In single crystal superalloys that are used for gas turbine blades, refractory elements such as Re and Ru are often added up to 10 wt% of the total [13–17]. The high temperature and the corrosive environments in which Ni-based superalloys often operate also induce detrimental phenomena at a micro-scale, such as the formation of undesired phases, γ' coalescence (with consequent depletion of reinforcing alloy elements) [18], degeneration of undesirable carbides, corrosion, and cracks [19–25]. These issues can be mitigated through a correct choice of chemical composition in relation to the use of the component.

Due to the high costs related to the production of components made of Ni-based superalloys, replacing damaged components might be prohibitive. Welding repair technologies, which are less expensive than part replacement, play an important role in extending their service life. Furthermore, given the geometrical complexity of some components, joining different parts by welding is convenient and sometimes necessary. In this scenario, the optimization of the welding techniques for wrought and additively manufactured components is of paramount importance, in compliance with the sustainability and cost reduction criteria.

The welding of Ni-based superalloys is challenging for both micro- and macro-structural aspects: they present crystallographic and chemical complexities that must be maintained over time under high-intensity solicitations (e.g., temperature and mechan-

ical stresses) that determine issues related to welding cracks, strain age cracking, alloy splitting, and porosity development.

Conventional welding methods for the repairation of Ni-based superalloy mechanical components such as turbine blades, vanes, and casings, involve often the use of gas tungsten arc (GTA) welding. A typical repair routine of a turbine blade implicates the removal of the damaged leading edge section and the welding of a “patch”, which is then machined and contoured to the original shape. This implies elevated costs and material consumption for the replacement of the damaged part. Moreover, components repaired via GTA tend to show high susceptibility to cracking due to large shrinkage stresses caused by the high heat input, and due to the embrittlement provoked by the large amounts of γ' rapid precipitation during the cooling phase [26]. The weldability of Ni-based superalloy is often evaluated based on the amounts of some alloying elements that might be detrimental. Several papers [27–32] report that Ni-based superalloys are generally very susceptible and, therefore, not weldable for specific contents of Al and Ti, as reported in Figure 1. Different empirical rules have been proposed. Sekhar et al. [33] reported that when the condition $2(\%Al) + (\%Ti) < 6 \text{ wt}\%$ is respected, the alloy is weldable. Alternatively, Haussman et al. [34] suggest maintaining the Al content below 6 at% and the (Ti + Ta + Nb + W) content below 8 at%. Al and Ti are the alloying elements involved in the formation of γ' phase. Indeed, Ni-based superalloys characterized by a low volume of precipitated phases or strengthened by solid solution are more suitable to be welded, whilst most precipitation-hardened versions can be welded with difficulty, showing cracking propensity during welding. For this reason, precipitated hardened alloys are often welded in solution-annealed conditions [35]. This issue is mainly related to the more complex grain boundary and lattice structure and the multitude of alloying elements [36]. Moreover, the heat generated during welding further contributes to the degradation of the bulk properties of the material and the precipitation of hardening phases.

Welding technologies with high energy density such as laser beam welding (LBW) and electron beam welding (EBW) are valid solutions to prevent some of the detrimental effects of traditional welding processes on Ni-based superalloys, improving the weldability thus reducing the cracking susceptibility of the heat affected zone (HAZ) [36].

High energy density techniques involve lower heat input than other welding techniques, with consequent effects on microstructure and mechanical properties. In particular, (i) lower heat input produces narrower seams, with a reduction of Fused Zone (FZ) and HAZ; (ii) rapid cooling rate reduced grain growth in HAZ and segregation; (iii) hindered formation of detrimental structures; (iv) more uniform heat distribution leading to lower residual stresses [37]. In particular, the rapid cooling rate in the FZ, typical of the high energy density welding techniques, affects the size of strengthening phases, such as carbides and γ' precipitates [38], and their morphology, evolving towards a rounder shape. The reduction in strengthening phase size and the finer structure causes an improvement in the mechanical properties of the weldment, i.e., hardness, tensile strength, and ductility [37]. Increasing the solidification rate helps to limit the detrimental phase precipitation in the altered microstructure, resulting in limited embrittlement of the welds and preventing the appearance of welding cracks. Moreover, these techniques offer the possibility to vary the process parameters in a wide range, therefore many combinations of parameters can be tested to optimize the microstructural and macrostructural features of the welded joints. Indeed, in this regard, interesting works [39–43] on modeling procedures and simulations by opportune physics-based and FEM models were also engaged in order to predict the seam shape, the distribution of the thermal field, the residual stress state, as well as the microstructural evolution (for example, in comparison to EBSD observations [37,44,45] during the processing and services.

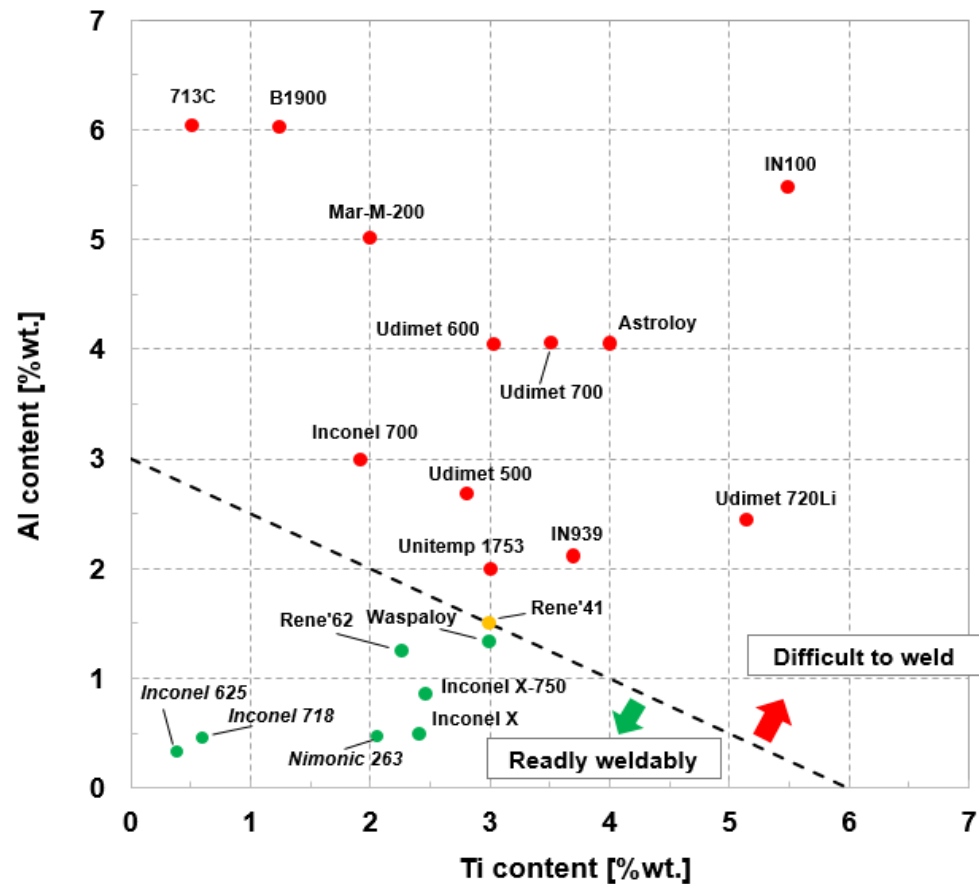


Figure 1. Weldability reference diagram for Ni-based superalloys depending on chemical composition (%wt.) Reprinted from ref. [33]. Copyright 2002 Sage Publications.

Despite the abundance of review papers available in the literature about nickel-based superalloy welding, to the best of the author's knowledge, there are none focused on high energy density methods. Hence, the present work aims to review the effort of the scientific community, specifically on the weldability of nickel-based superalloys via LBW and EBW, focusing on the description of the post-welding microstructural features and issues of the resulting microstructure in the FZ and HAZ, which determine the mechanical and electrochemical properties of the material. The next section presents a general introduction to the high energy density welding techniques (Section 2), followed by an explanation of the concept of weldability (Section 3). The processes LBW and EBW will be thoroughly described, reporting several examples of application to Ni-based superalloys (Sections 3 and 4). The final part of the review (Section 5) is focused on the following three Ni-based superalloys: the solid solution strengthened Inconel 625; the precipitated-hardened Inconel 718 with one of its variants, the AF955; and the γ' precipitation reinforced Nimonic 263. These alloys were selected for their potentiality and the high demand that exists due to their excellent performances.

2. High Energy Density Welding Techniques

To overcome the issues related to conventional welding processes, several works developed interesting investigations on the use of alternative welding processes such as the high energy density welding techniques Laser Beam Welding and Electron Beam Welding. It is often mentioned that those techniques are characterized by low heat input [46,47]. Indeed, the beam, whether electron beam or laser beam, can be considerably powerful, but it provides a very localized heat input, that limits the amount of melted material and

reduces the overall heat input that the joints face. This is beneficial from many points of view: first, the portion of material that is melted, the fusion zone, or altered by the heat, the HAZ, are reduced in volume, thus the cooling rate is fast, and the welds can be very accurate. This induces minimal distortion and minimal residual stresses on the joint. Moreover, it is possible to have better control of the segregation and modifications of the microstructure, especially for what regards the coarsening of the grain size. In addition electron and laser beams provide greater penetration depth, and high depth-to-width ratio in comparison to conventional processes [46–49], enabling single-pass welding. Single-pass welding routines are desirable not only for productivity reasons but also because multi-pass weldings imply repeated thermal cycles that are likely to induce inhomogeneous microstructure in the FZ with higher content of segregated carbides, coarser microstructure and thus decreased hardness [50]. The schematic in Figure 2 shows the different shapes and sizes of the typical cross-section of welds obtained with different methods, highlighting that EBW and LBW produce very narrow beams.

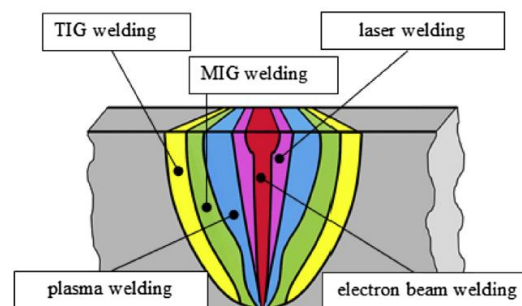


Figure 2. Schematic of the weld width with different welding techniques. Reprinted from Ref. [48].

Despite the high operational costs, the beam techniques are suitable for industrial applications. Since they are fast and accurate, they enable high productivity and are suitable to be integrated into automated production lines. Moreover, they allow design flexibility, and the welds can be done with or without filler materials (autogenous welding), reducing the consumable costs [51].

The schematics of the process and components required for the generation and use of laser and electron beams are shown in Figure 3. The LBW process involves the use of a monochromatic laser beam focused on the material to weld, generally protected from environmental contamination using inert gas, such as helium or argon. The beam energy is transferred into the material by conduction phenomena, and a hemispherical melted volume is formed: during the relative workpiece-laser beam movement, the material is locally subjected to continuous melting and solidification, forming a deep, narrow weld bead. Industrial laser beam power density can go up to approximately $10^8 \text{ W}\cdot\text{cm}^{-2}$ [46], but it can vary in a wide range of values, with many orders of magnitude of difference. Parameters such as beam power, beam spot size, and welding speed must be chosen according to the material to weld and the desired characteristics of the joint. Laser beam equipment is relatively less expensive and sophisticated than the EBW one, but some limitations on the applicability of LBW regard the strong influence of the surface preparation on the weld quality and possible issues related to the reflectivity of the laser on some materials [47].

Electron Beam Welding is performed in a vacuum chamber using a focused high kinetics energy electron beam as the heating source to melt and join metal parts. The electron beam is generated by a negatively charged filament (cathode) that is heated in its thermo-ionic emission temperature range: in this temperature range, electrons are emitted and then accelerated by the electric field between the cathode and the anode. The beam is

formed by channeling the electrons through an orifice in the anode [52]. The beam energy concentration can go up to 10^7 W/cm² [48]. Some of the process parameters that determine the quality of EBM joints are the beam current, the beam accelerating voltage, the focal beam spot size, the welding speed, and the vacuum level; the quality and characteristics of the desired joints depend on these parameters. Residual stresses, bulk distortions, FZ, and HAZ width can also be controlled through a proper tuning of the process parameters. Contrary to LBW, which offers the possibility to weld at atmospheric pressure, EBW requires a vacuum chamber, which poses extra costs and limitations. The chamber volume restricts the size of the weldable components, hindering the diffusion of EBW as an industrial solution. Nonetheless, the chamber prevents gas contamination in the joints and protects the melt pool from the atmosphere avoiding oxidation. Other limitations of EBW are related to the reactivity of the electrons with metal materials, leading to the generation of dangerous X-rays, and to the possible interaction with magnetic materials [47,48,53].

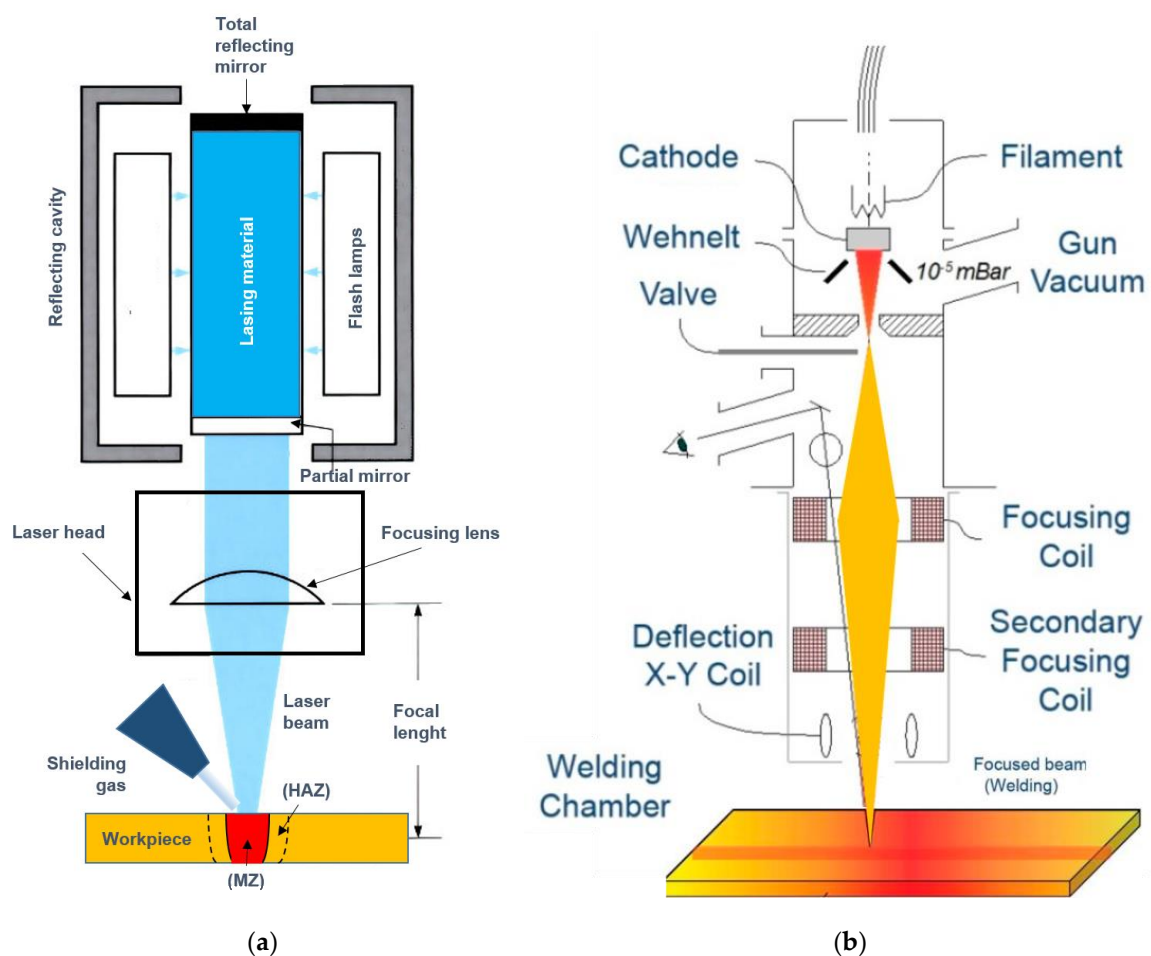


Figure 3. (a) Sketches of Laser Beam Welding, and (b) Electron Beam Welding processes. Reprinted from Ref. [54].

3. Weldability of Ni-Based Superalloys

The weldability of an alloy defines whether it is possible to obtain welded joints with good integrity and mechanical properties [55]. Indeed, in the case of Ni-based superalloys, the concept is often reduced to the evaluation of the crack susceptibility [56]. The multitude of parameters that affect the cracking susceptibility can be divided into four categories: base material characteristics, welding process parameters, parts geometry, and filler material properties [56]. The most typical cracking mechanisms occurring in Ni-based superalloys

are liquation and solidification cracking, although some other mechanisms have been recognized and described in the literature.

Liquation cracking is associated with thermal cycles and large thermal gradients, leading to microstructure gradients and generating a large stress region. The liquefaction of segregated alloying elements (Ti, Nb, and Al), and the formation of low melting constituents create a liquid film at grain boundaries in the HAZ, hindering the densification of the material. This tendency is enhanced by high heat input during the welding and by coarse microstructure [55]. Moreover, mechanical issues are at the base of HAZ cracking during welding: indeed, the high hardness of the base material can affect its capability to relieve part of tensile stress during weld cooling on the HAZ liquated grain boundary. These phenomena can be increased by stress concentrations due to γ' precipitation that further hardens the microstructure.

Solidification cracking takes place during the last stage of solidification: the remaining liquid along the grain boundaries or in the interdendritic regions solidifies before the volume reduction occurs, due to the solidification of the material, meaning that the remaining shrinkage is not accommodated. Usually, solidification cracking occurs at the centerline of the fusion zones of the joint and it depends on microstructure and alloying elements. Limiting the formation of intermetallic compounds and carbides is a possible strategy to reduce the crack susceptibility of the alloy [55].

It must be noted that Ni-based alloys that are strengthened via precipitation hardening are also susceptible to strain age cracking (SAC), which occurs during the service life of the component or during post-welding heat treatment when a high temperature is reached. The phenomenon is due to the inability of the grain boundaries to accommodate the internal stress resulting from the precipitation of gamma prime [35,36,55], and it is correlated to the amount of Ti and Al in the alloy. To conclude the overview of the cracking mechanisms affecting welded superalloys, ductility-dip cracking (DDC) is another mechanism that has been described as a propagation of the liquation crack phenomena at lower temperatures [27,35]. It is seldom reported since it is not very common in Ni-based superalloys.

The cracking susceptibility depends on many parameters. It is sometimes reported that welds obtained via high-energy-density techniques are more prone to cracking than conventional welding processes [47,57]. Nonetheless, these techniques allow better control of the heat input, thus controlling the amount of segregation and precipitates at the grain boundaries, which are considered the main reasons for the crack susceptibility [26]. The grain size distribution is another important factor in the formation of welding cracks [27]. In particular, liquation cracking is claimed to be favored by coarse grain size in the HAZ [35], and grain refinement is also suggested in [58] as a strategy to reduce solidification cracking. Coarse grain might be beneficial to enhance the creep resistance, reducing the grain boundary sliding phenomenon [59], but this is true only for very high-temperature applications, depending on the fracture mechanism activated (i.e., intragranular or intergranular) [60]. Moreover, finer microstructure is, in general, beneficial for the tensile properties, microhardness, and oxidation resistance of the alloys [61].

Several papers demonstrated that the grain size distribution and the grain boundaries morphology obtained after welding processes are mainly related to the molten pool thermal characteristics, as the temperature gradient (G) and the solidification rate (R) (or velocity), usually combined in the parameters ($G \times R$), which is the cooling rate, and G/R , as shown in Figure 4: they influence the grain size and the morphology of the solidified microstructure, respectively [61,62]. Investigations on IN718 [63] and Renè 77 [26] underlined these aspects as fundamental to define the correlation between the desired microstructure in the fusion zone and the laser parameters: if G/R rises, the solidified microstructure will be planar, with columnar or cellular grains, whereas lower G/R leads to dendrites or equiaxed

dendrites [62]. G and R are claimed to be dependent on both welding speed and heat input: increasing welding speed and heat input reduces G/R , which in turn induces grain refinement in the fused area [64,65].

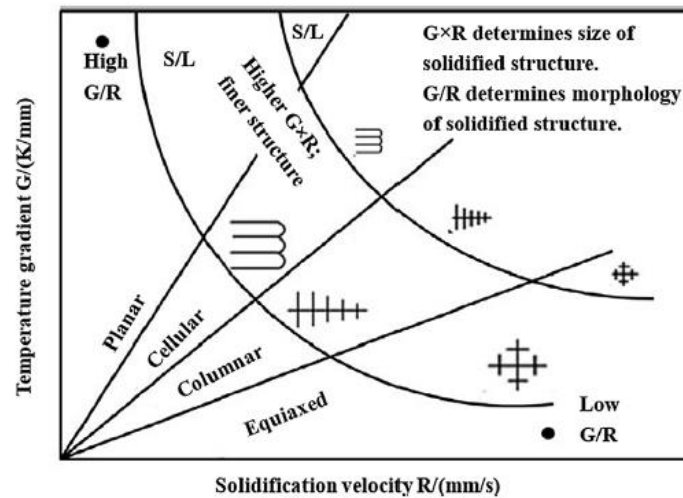


Figure 4. Influence of G and R parameters on the possible resulting solidified microstructure. Reprinted from Refs. [52,53].

The thickness of the joints is known to affect the quality of fusion welds, including EBW and LBW. When conventional arc-welding processes are employed, thick sections entail additional issues due to the multiple passes required and the use of an increased amount of filler material [50]. Besides the additional costs and productivity issues, multipass weldings are connected to porosity formation, bead distortion, and hot cracking susceptibility. High-energy-density welding processes are capable of greater penetration depths, which allow better control of the weld quality and reduce crack susceptibility. This is demonstrated in [50], where single-pass laser welding of thick sections of IN617 was proven to be feasible, providing homogeneous and refined microstructure and superior mechanical properties in comparison to multi-pass GTA welding and hybrid laser welding.

Most of the research considered in the present review investigated autogenous welding, although it is reported that the filler material has a beneficial effect on the compensation of material loss due to vaporization, minimization of the underfill [66], alleviation of thermal stresses, hence reduction of the FZ cracking tendency [67,68]. Nonetheless, the propensity of superalloys to HAZ cracking is difficult to limit when filler materials are employed, and it is required to carefully control its chemical composition. For example, it is reported that a lower concentration of Ti and Al and a small mismatch between the γ and γ' phases are advantageous [69,70], even though this might come at the cost of reduced mechanical properties in comparison to the base material.

4. Laser Beam Welding (LBW)

Laser beam welding has drawn attention because of its potentiality and the abovementioned advantages over traditional welding techniques. Many investigations are focused on the differences between the most used laser typologies to evaluate the corresponding effects on the macro- and micro-structural features of Ni-based superalloy welded components. Many types of lasers exist, and they are often referred to based on their active medium, such as gas laser or solid-state laser. A typical gas laser that was commonly used in the past for welding applications is the CO₂ laser, although nowadays solid-state lasers are more used, such as the Nb:YAG laser [47]. Recently, fiber lasers have gained popularity since they allow fast welding and are known for their great stability and accuracy [71].

In a comparison proposed by Ren et al. [72], the fiber laser showed increased melting efficiency and lower minimal heat input required for full penetration welds of Inconel 617 butt joints in comparison to the CO₂ laser. Nonetheless, gas lasers were successfully used to weld different superalloy joints such as Inconel 625 [38], Inconel 718 [73], and Nimonic [74]. Some examples of applications of the Nd:YAG laser can be found on Inconel 718 [66], Inconel 600 [75], and NiTi shape memory alloy [76]. The Nd:YAG laser was proven to create better quality joints in comparison with other laser types. Gobbi et al. [77] observed higher uniformity of the beads in Inconel 718 joints welded with the Nd:YAG laser in comparison to gas laser. This entails lower residual stresses and no microfissuring, which is a critical issue of laser welding that will be addressed in the following section. In general, Nd:YAG laser has various advantages related to the high-energy absorption rate due to a low reflectivity, a high welding speed, and low residual stress compared to CO₂ laser [78]. These advantages make the Nd:YAG laser more convenient and suitable for on-site operation and factory automation for high-volume production in several industrial applications [78,79]. These comparisons are significantly influenced by the choice of the laser parameters. It must be noted that these comparisons are significantly influenced by the choice of the laser parameters, by the pre-welding conditions and the post-welding heat treatments.

Indeed, a proper optimization of the laser welding parameters is required to guarantee the quality of the welds. Many researchers performed ANOVA analysis or DOE methods [38,66,80–82] to determine the best parameter combinations. As mentioned earlier, the most important parameters are laser power and welding speed, but other aspects deserve attention, such as shielding gas flow rate, shielding gas pressure, focal position, and frequency of pulsation. For example, about the latter, it was observed in [83] that laser frequency is an important factor to consider since Hastalloy X joints obtained with pulsed Nd:YAG laser beam were significantly less porous in comparison to joints obtained with a continuous fiber laser. Similarly, the contribution of Jiang et al. [84] proposed a comparison between continuous (CW) and pulsed waves (PW) fiber laser welding of GH3535 superalloy, demonstrating that lower seam quality was obtained in CW mode than in the PW, with consequent negative effects on the mechanical properties of the welded components. Reduced porosity was observed in the PW joints, where the local CO micro-voids in the melting pools are effectively removed by the subsequent pulse. Increasing the laser beam frequency with the correlated intensification of the stirring in the melting pool enables even lower porosity levels.

Several studies available in the literature investigated the correlation between laser parameters, microstructure alteration, and crack susceptibility in an attempt to reduce the issue of welding cracks in Ni-based superalloys. One of the possible strategies to adopt in the case of high crack susceptibility is the application of a suitable heat treatment before welding, inducing a more homogeneous dispersion of precipitates, reducing the thermal gradients, and altering the hardness of the base material [31]. Another solution can be the use of a ductile filler metal [31,66,69,85]: to reduce the micro-cracking phenomena associated with repairing operations of turbine blades, a filler alloys having lower Al and Ti concentrations than the base material can be used [69,85]. The issues related to the use of filler material were previously discussed.

An interesting contribution proposed by Zhu et al. [86] underlined the evolution of the microstructural feature along the fusion line between the FZ and the HAZ of the laser welded polycrystalline GH909 superalloy, focusing on the formation process of γ /Laves eutectic constituents on the laser welds: the sketches in Figure 5 show an interesting schematic representation [86] of the solidification process and the formation mechanism of Laves eutectic constituents and grain boundary liquation in the FZ and HAZ, respectively,

that are considered the primary causes of liquation cracking. The liquation of Nb-rich MC carbides (Metallic Carbides) in welded Ni-based superalloys is pointed out as one of the most important reasons for HAZ microfissuring.

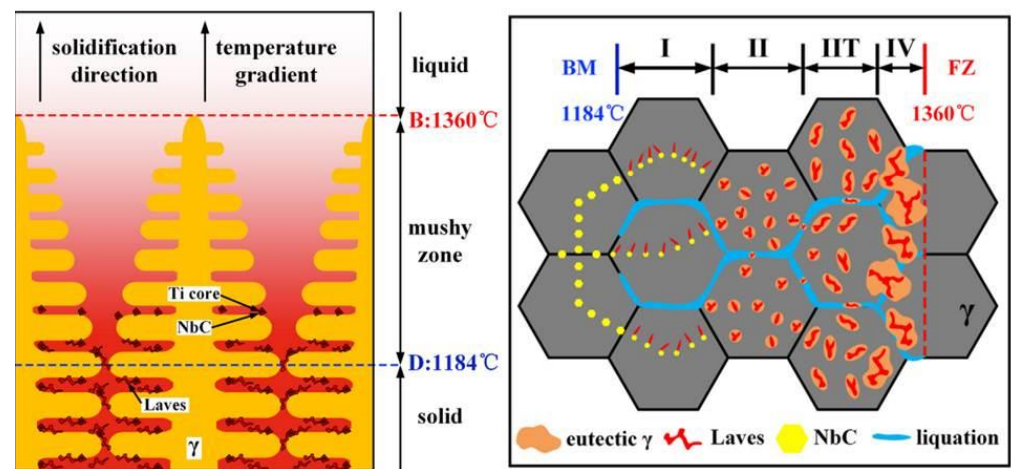


Figure 5. Representation of the solidification processes and constituents formation in FZ (equivalent to melted zone MZ) and HAZ of GH909 Ni-based superalloy. Reprinted from Ref. [86].

Montazeri et al. [31] also showed the association of the HAZ cracking with the liquation of grain boundary constituents such as γ - γ' eutectics, carbides, Cr–Mo borides, and Ni–Zr intermetallics (Figure 6). In their work, different pre-welding heat treatments were performed, demonstrating that the hardness of the base material and the dissolution of the abovementioned grain boundary constituents play a significant role in the crack susceptibility of the joints.

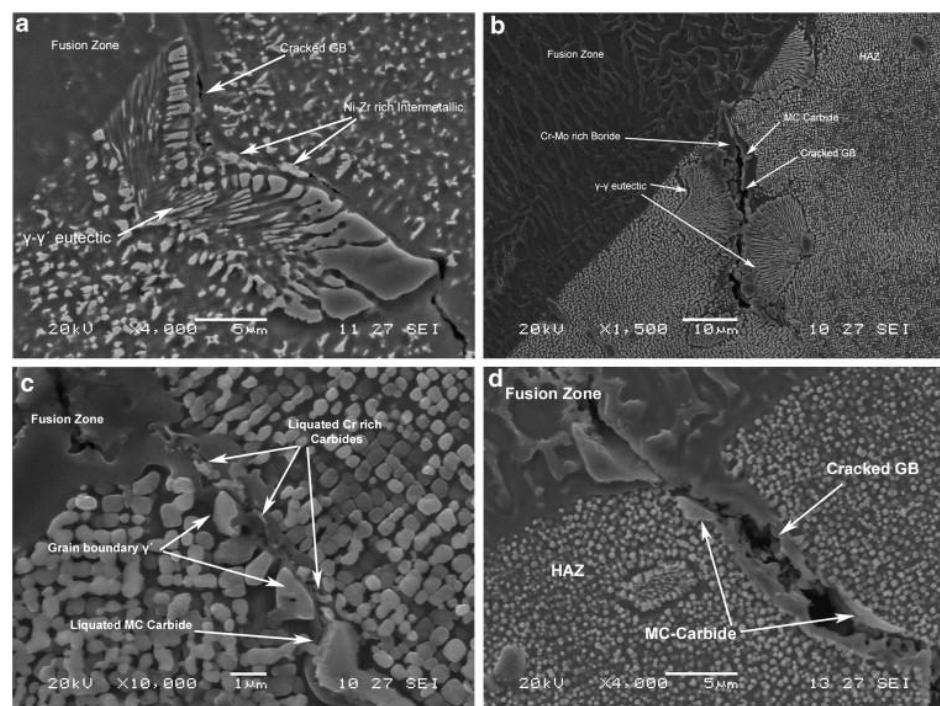


Figure 6. Constituents formation in the fusion zone in an IN738 Ni-based superalloy by Nd:YAG pulsed laser welding process. Reprinted from Ref. [31]. HAZ liquation cracks associated with: (a) Ni–Zr intermetallic, (b) γ - γ' eutectic and Cr–Mo boride (c) Cr rich Carbides and (d) Ta rich MC carbides.

Grain boundary liquation is claimed to originate from the heat input during the welding and consequent grain coarsening [86,87]. In [87], solid solution GH909 specimens were welded using a fiber laser. The investigation of the joint microstructure revealed that larger grains are more prone to precipitation and segregation, incrementing the liquation at high temperatures of lower melting constituents. As already stated, reducing the laser power and, with a minor effect, the welding speed is beneficial in preventing liquation cracking [87]. Liquid film formation on the grain structure in the HAZ is also observed by Ojo et al. [88], who presented an exhaustive study on the HAZ characteristics of IN738 cast superalloy, underlining the presence of grain boundary γ' liquid. Interestingly, the formation of this damaging phenomenon was not observed by Osoba et al. [89] on the Haynes282 autogenously welded by single pass CO₂ laser beam: the absence of the responsible γ - γ' eutectic transformation constituents was explained by the modified primary solidification path through C addition, whilst Ti and Mo rich MC-type carbide are observed on the FZ (Figure 7). Inconel 800, which is particularly suitable for aggressive corrosive environments was extensively investigated in [90], revealing that grain refinement and minor Laves phase precipitation are achievable by increasing the scanning speed, since the heat input is reduced and the cooling rate enhanced.

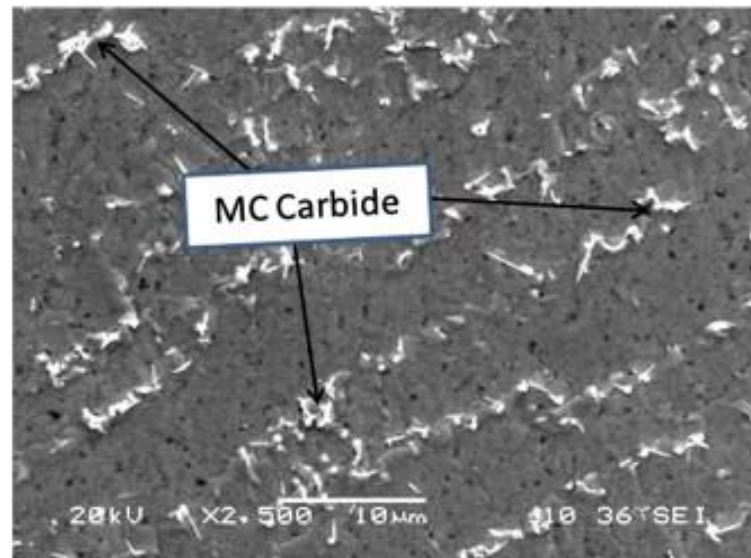


Figure 7. Details by scanning electron micrograph for the microstructure of the FZ in a Haynes282 welded by CO₂ laser beam. Reprinted from Ref. [89].

Regarding the solidification cracks, multiple studies demonstrated that they are usually located at grain boundaries and, therefore, are affected by the grain boundary energy (γ_{gb}). The latter depends on the misorientation angle (θ) and alloying elements, influencing the crack susceptibility [91]. In fact, if $\gamma_{gb} > 2\gamma_{sl}$ (solid-liquid interfacial energy), a transition from attractive to repulsive grain boundary occurs and the liquid film at the grain boundary becomes stable, hindering the coalescence of the dendrites and favoring the hot cracking appearance. The dendrites coalesce occurs with a certain undercooling ΔT_b (θ) that increases with the misorientation angle (θ). When θ increases above a critical value (θ_c), a high localization of strain appears with consequent solidification cracking [92]. Nrouzian et al. [58] proposed several strategies to avoid solidification cracking including grain refinement and the oscillation of the laser, that can create more turbulence in the melted pools favoring fine grain nucleation. A schematic of the formation of solidification cracks is shown in Figure 8.

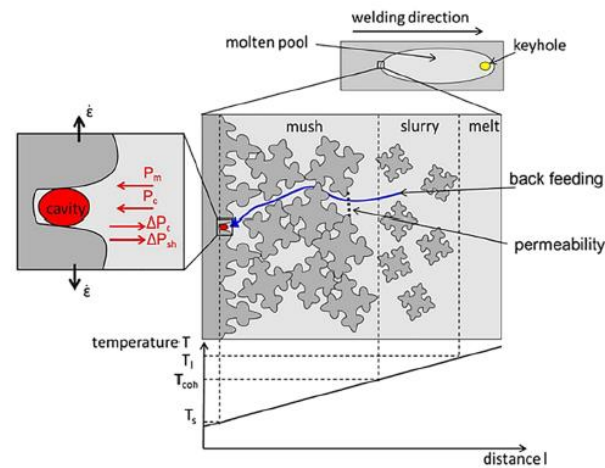


Figure 8. Schematic of solidification cracking formation. Reprinted from Ref. [58].

Important applications of LBW regarding the aeronautical sector and power energy plants involve components such as turbine blades. To increase the creep resistance of Ni-based superalloy turbine blades during high-temperature applications, single-crystal or directionally solidified microstructures are often evaluated as well as the role of the crystallographic orientation on the alloy susceptibility. Fusion welding of single crystal alloys poses some issues related to the possible presence of stray grains in the FZ, which are often associated with cracks [93], as shown in Figure 9. The picture shows several stray grains in the center of the FZ of a PWA 1480 single crystal weld obtained by pulsed laser, and a crack along stray grain high angle boundaries is visible. The constitutional supercooling ahead of the advancing solidification front is indicated as the formation mechanism of the stray grains. In particular, refs. [93,94] underlined the dependency of stray grains formation on the laser parameters since the issue can be avoided by reducing the laser power and the welding speed.

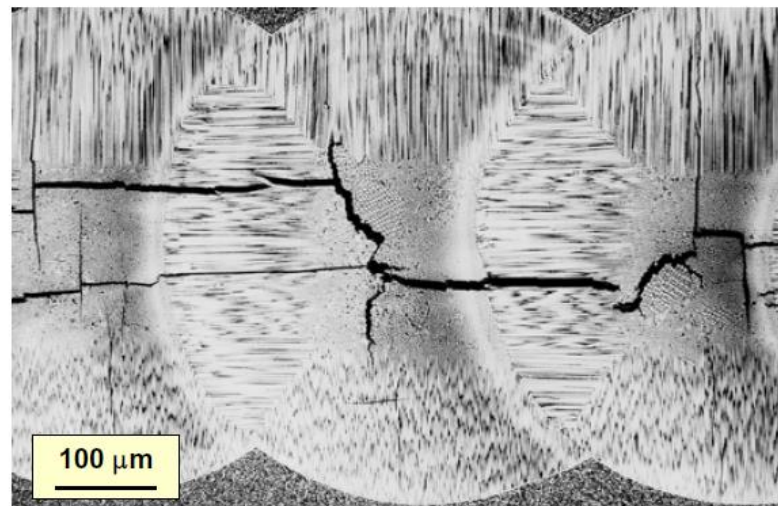


Figure 9. Pulsed laser weld on PWA 1480 single crystal Ni-based superalloy showing large regions of epitaxial growth as well as abundant stray grains and cracking along stray-grain high angle boundaries. Reprinted from Ref. [94]. Copyright 2004 The Minerals, Metals & Materials Society.

The nature and distribution of the micro-constituents that can be obtained by a LBW process on single-crystal Ni-based superalloys were also investigated by Wang et al. [95] on the solution heat treated CMSX-4 and the partial solution heat treated CMSX-486 superalloys: W and Re segregation into the dendrite regions were individuated whilst Ti,

Ta, Al (γ' forming elements) and Hf in the interdendritic regions were observed, as well as Chinese script carbides in CMSX-46. Stray-grains presence was also confirmed, especially in CMSX-486 because of the Hf, Zr, and B segregations in the liquid phase. The effect of the pre-weld conditions is, therefore, minor than the chemical composition effect.

5. Electron Beam Welding (EBW)

Electron beam welding produces a seam characterized by deep penetration, narrow FZ and HAZ, and low residual stresses due to more uniform heat distribution, which makes EBW joints potentially superior in comparison to traditional welded counterparts. For example, the comparison on IN825 proposed in [53] revealed that EBW joints are overall better in comparison to GTAW welds, where the elevated heat input led to the formation of coarser microstructure and cracks (Figure 10). Nonetheless, when process parameters are not optimized, it is difficult to obtain crack-free welds. This is particularly challenging in single crystal alloys: Curchman et al. [96] compared the welds obtained on a single crystal alloy with EBW and conventional GTA, reporting that GTA welds were generally crack-free, while in the EBW welds stray-grains were present, inducing cracks.

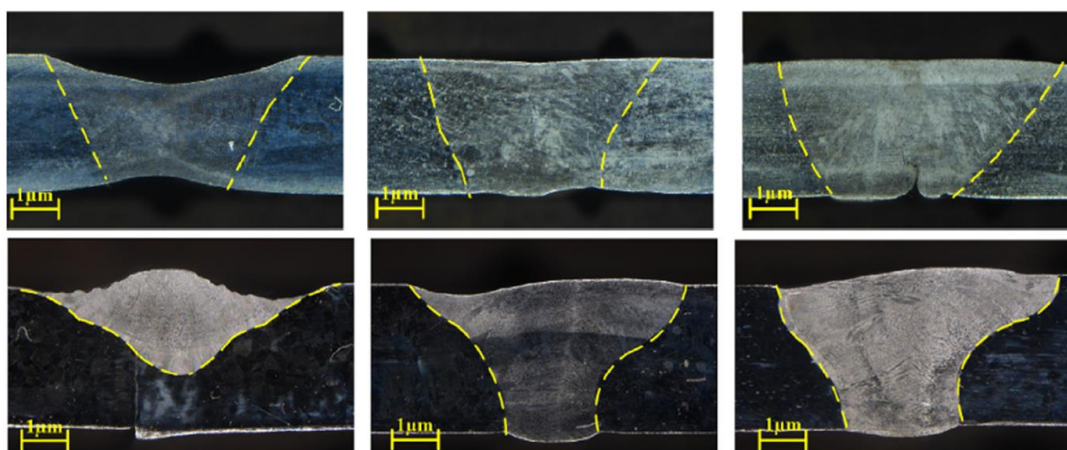


Figure 10. Comparison between the cross-sections obtained by GTAW (first row) and EBW (second row) varying the process parameters. Reprinted from Ref. [53].

As mentioned before, the peculiarities of the EBW process, such as the necessity of the vacuum chamber, entail higher quality of the joints, even in comparison to LBW. Sekhar et al. [33] proposed an interesting investigation on laser and electron beam welding of thick joints made of two very popular superalloys in the field of gas turbines in full heat-treated conditions, that are the precipitation-strengthened Waspaloy and Udimet 720Li. Their results highlight that the EBW joints are less porous, although more distortion occurred in the joints. Moreover, from the reported pictures of the cross-section of the welds, it is possible to notice the difference in the shape and dimensions of the fusion zone.

To find the optimal parameters and obtain microstructure and mechanical properties as close as possible to those of the original material, many investigations start with an optimization procedure that entails testing different parameter combinations [80,97]. The parameters affecting the process are divided into two groups according to [98]: beam parameters (e.g., accelerating voltage and beam current) and welding joint features (e.g., welding speed, welding width, vacuum pressure, and preheating temperature). Statistical tools can be used to combine the parameters effectively, as in [99]. For example, Choudhury et al. [100] used the RSM-JAYA algorithm to combine different values of beam current, accelerating voltage, welding speed, and beam oscillation, revealing that the accelerating voltage, followed by beam current, has the main impact on both penetration and width

of the beam. The beam oscillation was found to be less relevant, although, in another study on Inconel 718 welded by EBW in solution-treated condition [101], it was proven to affect the crack susceptibility: the elliptical beam oscillation that was employed reduced Nb segregation and amount and morphology of the Laves phase in the interdendritic region and determined positive improvements in tensile strength and ductility. The welds were subjected to different post-welding heat treatments revealing that the elliptical beam oscillation determined positive improvements in tensile strength and ductility at room temperature independently of the heat treatment.

Welding speed and heat input are the main responsible for the definition of the grain size with consequent effect on the crack susceptibility [102,103].

The typical microstructure observed in EBW Ni-based alloy joints is characterized by the formation of equiaxed dendrites in the center of the FZ and a transition from cellular to columnar dendrites near the HAZ, as shown in Figure 11 [37,53,104–107]. In general, the microstructure is always finer than the one obtained with other welding techniques, and this theoretically leads to higher hardness and tensile strength. Nonetheless, other factors might play a relevant role, such as the amount of δ -precipitates as a consequence of heat treatments, as reported in [106]. The reason behind the grain refinement is the lower heat input that characterizes the EBW process in comparison to others [108]. The fine microstructure was also observed in single crystals Ni-based superalloy joints where the microstructure transforms into polycrystal [102] after EBW.

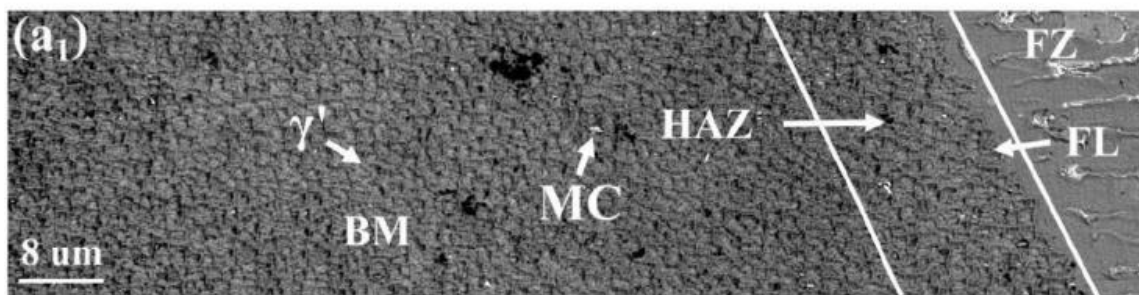


Figure 11. Typical microstructure of an EB weld. Reprinted from Ref. [107].

Solidification and liquation cracks in the FZ and HAZ are mainly correlated to the precipitation of phases such as γ - γ' eutectic, Cr-Mo boride, Ni-Zr intermetallic, MC carbide, and γ' phase, as reported in [109] for IN738. In [110] it is reported that liquation cracking in solutionized K465 nickel-based superalloy is also favored by the segregation of elements such as Ti, Nb, and Al, in addition to the phases previously mentioned. B segregations are also considered responsible for crack susceptibility in Ni superalloy 718. It was proven in [109] that increasing the beam current is beneficial since the higher heat input contributes to the reduction of residual stresses related to the cooling of the welds. Moreover, increasing the beam current improves the backfilling mechanism, which entails the filling of a crack due to the melted material in the fusion zone that moves backward for capillarity [111]. A schematic of a typical process of solidification of the superalloy GTD-111 is represented in Figure 12, to highlight the segregations that are at the origin of solidification cracking [112].

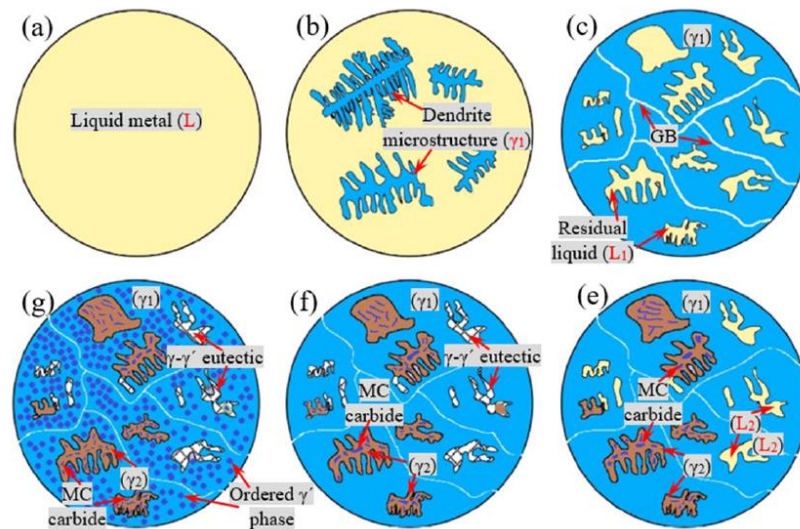


Figure 12. Schematic of the solidification process of GTD-111 nickel-based superalloy. Reprinted from Ref. [112]. Schematic of GTD-111 superalloy solidification steps, (a) Liquid metal, (b) Formed dendrite structure (γ_1), (c) The residual liquid in IDR, (e) Precipitation of MC carbides, (f) Formation of γ - γ' eutectic, (g) precipitation of ordered γ' phase.

Crack susceptibility not only depends on the heat input, but it also worsens with the reduction of the welding speed [92,110]. The number and length of transverse cracks increase with the reduction of welding speed due to: (i) the segregation at grain boundaries of some alloying elements producing an increased volume of liquid film and (ii) the transformation of low-angle grain boundary (LAGB) into high angle grain boundary (HAGB). According to previous research [91,92], this results in a higher cracking susceptibility. Moreover, the average grain size of the joint decreases with the welding speed with changes in the mechanical properties, such as the microhardness of the fusion zone.

Besides the optimization of the process parameters [101,102] discussed previously, several strategies are proposed in the literature that can be adopted to reduce cracking susceptibility by (i) controlling chemical composition in the weld [104,107,113], (ii) filling a deposited layer [107,114], and (iii) employing pre-heating or post-welding heat treatments.

An example of chemical composition control (strategy (i)) can be found in [104], where crack formation in GH4169 alloy can be inhibited by adding Mn, since it promotes the formation of the high-melting phase Mn_2Nb , avoiding the formation of the low-melting phase Ni_3Nb at the grain boundaries. Similarly, the beneficial effect of C addition on the cracking susceptibility of the DS TMS-75 superalloy depends on its ability to promote the MC formation in the $L \leftrightarrow \gamma + MC$ reaction, reducing the amount of liquid available for the γ - γ' eutectic transformation [113].

The control of the chemical composition can be done by taking action on the joint design (strategy (ii)). For example, Sun et al. [107] designed a sandwich structural joint of IC10 with Inconel718 alloy single crystal deposited layer with a higher amount of Cr and Nb. The strategy was able to solve the cracks problem in the IC10 EBW joint. In fact, the presence of an additional deposited layer changes the microstructure of the weld and, in particular, the amount of some elements (Al, Cr) that can influence the grain growth and precipitated phases.

Among the alloying constituents, Al is one of the elements that shows the most intense effect in the promotion of the columnar-to-equiaxed transition (CET) [115]. Therefore, by filling a deposited layer with a lower amount of Al, with respect to matrix composition, it is possible to promote columnar dendrite microstructure that improves the plastic deformation because of better resistance to tension than that of the cellular dendrite [107,116]. The

deposited layer influences also the type of precipitated phases, because of the tendency of C to preferentially form carbides with Nb instead of Ta due to the different enthalpy. NbC has a higher melting point and can avoid the generation of liquid film in the intergranular region preventing cracking [117].

Finally, another strategy to prevent cracking (iii), is the use of pre-heating, which reduces temperature gradient and micro-segregation. By adopting the optimal pre-heating, weld seams without defects can be obtained [54,118]. To reduce segregation and uniform microstructure in the weld, post-welding aging treatments can be employed [116]. They also promote the precipitation of δ -phase [106], spherical γ' [101], and Cr-based MC-type carbides [37] and reduce the strain concentration in the weld [116], with consequent improvements in tensile properties.

These strategies also affect the mechanical properties of the welded joint: for example, the addition of Mn, which inhibits the crack formation in GH4169 superalloy, also prevents the formation of macroscopic defects resulting in good mechanical properties of the joint, although yet not comparable with a base material properties (tensile strength 743.7 MPa, Vickers hardness > 300 HV) [104]. Indeed, the welded joints' mechanical properties are usually worse in comparison to the virgin materials. For example, an analogous reduction in mechanical properties has been observed in welded joints of Inconel 718: tensile strength, yield strength, and elongation of the whole joint at 650 °C on average are 90%, 80%, and 80% of parent material, respectively. Moreover, it must be noted that the properties vary from the top to the bottom of the seam, with maximum values and brittle fracture features observed on the top side, and lower values with ductile fracture features on the bottom side [106]. In general, the volume fraction of precipitates in HAZ is higher than in the parent metal, and increases with the heat input, resulting in higher hardness and strength and lower ductility and toughness [119]. The effect of interdendritic precipitation on mechanical properties has been observed also for Inconel 825 and 686 Ni super-alloys [66,69]: the presence of secondary phases (Al_4C_3 and TiN in the first case) and the segregation of Mo and W at grain boundaries improve tensile properties but can reduce corrosion resistance, ductility and impact toughness of the weld.

6. Typical Ni-Based Superalloys in Detail

In order to highlight the effects of the LBW and EBW processes on the microstructural properties of peculiar superalloys, the description is now focused on three polycrystalline Ni-based superalloys, characterized by different strengthening mechanisms.

6.1. Inconel 625

The chemical composition of Inconel 625 (IN625) is reported in Table 1.

Table 1. Chemical composition of Inconel 625 (%wt).

C	Co	Cr	Mo	Ti	Si	Fe	Mn	Al	Nb + Ta	Ni
0.1 max	1.0 max	20–23	8.0–10.0	0.4 max	0.5 max	5.0 max	0.5 max	0.4 max	3.15–4.45	Bal.

Inconel 625 is a Ni-based superalloy strengthened mainly by solid solution with Nb and Mo [120], although the alloy can also be strengthened by precipitation [121–123], mainly due to fine metastable phase γ'' (Ni_3Nb), which has D0_{22} crystallographic ordered structure after annealing in the temperature range between 550 and 850 °C [123]. Thanks to its corrosion resistance at high temperatures, it is also used as a cladding material on carbon steel and stainless steel.

The metastable structure γ'' transforms into the orthorhombic phase δ ($\text{Ni}_3(\text{Nb}, \text{Mo})$) after prolonged exposure to high temperatures [17,124,125]. The content of C and Cr also has significant effects on the mechanical properties, as it induces the precipitation of different types of metal carbides (M_{23}C_6 , M_6C , and MC) that develop with exposure at temperatures between 1033–1253 K [126]: indeed, MC are primary carbides that decompose into M_{23}C_6 and M_6C depending on the aging time and temperature. In addition to the excellent surface stability and excellent resistance to oxidation and corrosion, Inconel 625 has a remarkable resistance to yield, creep, and fatigue, finding wide use in many different applications from cryogenic conditions to high temperatures above 1000 °C [127–130]. Furthermore, IN625 is considered one of the superalloys characterized by higher weldability and workability [131], due to the low concentration of Ti and Al. It has been widely used in aerospace, chemical, petrochemical, and marine applications.

Some examples of parameter optimization can be found in [131] with a Nd:YAG, and in [38], with a CO_2 laser beam, where the importance of the correct choice of the heat input is highlighted. In [131] the Response Surface Method is used for the optimization, and the microstructure obtained shows a fully dendritic arrangement in the FZ, with dispersive precipitation in the interdendritic regions. It was observed that the hardness of the seam increases with increasing heat input because of Si, Mo, and Nb segregation at the grain boundaries, with consequent formation of Laves phases and NbC carbides. Those phases affect significantly the weldability of the alloy and deteriorate its resistance to liquation and solidification cracking [131]. In [38] the shielding gas flow was also taken into account alongside laser power and welding speed, although its impact was limited. The parameter combinations were obtained from a DoE, and the heat input was found to control the penetration depth, the residual stresses, and the porosity in the seam. These results are corroborated by other similar studies, as in [132]. With regards to mechanical properties, the correct choice of the parameters permitted to obtain welded joints with final mechanical properties comparable to the values obtained for bulk material in [38]. Indeed, according to [41], the tensile properties of the welds can increase with decreasing laser power since a finer microstructure can be obtained in the fused zone. According to [133], increasing the welding speed also helps in reducing the grain size, thus improving tensile properties.

Inconel 625 shows good weldability not only in the LBW process but also when an electron beam is employed. Welds free from welding cracks and HAZ microfissuring were obtained in [134,135], where the good EB weldability of IN625 was confirmed. Moreover, in [135], a thermal numerical model of the EBW process was developed, by adopting a superimposition of two different power density distribution functions (spherical heat source and conical heat source). Electron beams can be employed in strengthening surface treatments, as in [136], where it was found that the focus current is a paramount parameter to determine the microstructure and wear resistance of the metals. It is important to mention that EBW is often considered a potential solution for the welding of dissimilar materials. For example, IN625 was successfully welded with stainless steel 304 L [137], the duplex stainless steel UNS 32205 [138], and cast 9%Cr steel (CB2) [139].

The following tables report some of the parameters that have been used in the literature to weld IN625 with LBW (Table 2) and EBW (Table 3). The studies reported belong to different categories: some works involve optimization procedures to identify optimal parameter combinations; others investigate the effect of specific parameters; and some others develop numerical models that require extensive experimental campaigns for the validation. All the contributions are useful to better understand the correlation between process parameters and microstructure-mechanical properties of the welds.

Table 2. LBW parameters for IN625 and corresponding references.

IN 625-LBW					
Ref.	Laser Types	Thickness [mm]	Laser Power [W]	Welding Speed [mm/min]	Comments
[131]	Nd-YAG	0.5	260	72	Optimal parameters to maximize weld strength with spot size 180 μm
			230	360	Optimal parameters to minimize microhardness with spot size 540 μm
[133]	Fiber	5	5000	1500–1800–2100	Study on the welding speed effect
[132]	Diode	0.7	800–1000–1200	1200–2100–3000–3900	Study on the heat input effect
[42]	Fiber	1.5	300–350–400	300–400–500	Numerical investigation
[41]	Nd-YAG	1.5	75–100–120–130	90–120–180–240	Numerical investigation
[38]	CO ₂	5	3000–3300	1000	Optimal parameters to achieve full penetration

Table 3. EBW parameters for IN625 and corresponding references.

IN625-EBW					
Ref.	Thickness [mm]	Acc. Voltage [kV]	Current [mA]	Welding Speed [mm/min]	Comments
[134]	5	60	100	1500	Study on the effect of grain boundary precipitation
[135]	2.5	150	15–14.5	720	Numerical investigation
[136]	10	60	10	240	Study on the beam focus current effect

6.2. Inconel 718 and AF955

Inconel 718 (IN718) is claimed to be the most used Ni-based superalloy in supercritical conditions applications. The chemical compositions of the standard IN718 (UNS N07718) and a variation of it, the AF955 alloy (patented by Acciaierie Foroni S.p.A.), are reported in Table 4 below. AF955 has a composition similar to IN718, with the difference of a quantity of Mo of about 5–6%wt., which is almost double of a typical IN718 (c.a. 3 wt%). Like IN718, the superalloy AF955 is strengthened by γ'' (Ni₃Nb) and γ' (Ni₃(Al, Ti)) phases precipitation in the γ matrix, with volume fractions of approximately 16% and 4%, respectively, after appropriate heat treatment [140]. Interestingly, there is almost no literature available about the application of high energy density welding processes, for instance. This kind of superalloy finds important applications in the oil and gas extraction industry because of the excellent corrosion resistance due to Cr, Al, and Mo content.

Table 4. Chemical composition for standard Inconel 718 (IN718) and the AF955 superalloy (%wt).

	Ni	Cr	Mo	Nb(+Ta)	Co	Ti	Al	Si	Mn	C	P	S	Fe
IN718	50.0– 55.0	17.0– 21.0	2.80– 3.30	4.75– 5.50	1.00 max	0.65– 1.15	0.20– 0.80	0.35 max	0.35 max	0.08 max	0.015 max	0.015 max	Bal
AF955	57.4	21.6	5.88	4.80		0.86	0.43	0.09	0.08	0.015	0.0086	0.0002	Bal

IN718 is a Fe/Ni-based superalloy that is a precipitation age-hardenable alloy widely used for applications in aircraft engines, energy power plants, marine, and in the oil and gas fields [17], where metallurgical stability is fundamental to fulfill the necessary combination of good mechanical and anti-corrosion properties, ensuring stability at high temperatures and pressure. It is characterized by γ'' (Ni₃Nb) phase as the principal strengthening precipitate, as for the IN625, but also by the precipitation of the γ' (Ni₃Al, Ti) phase. The first one is a metastable phase that can evolve to the more stable and incoherent δ phase after prolonged exposure to temperatures above 650 °C, as mentioned in the previous sections: for this reason, IN718 superalloy maintains high creep and fatigue strength at high temperatures up to the aforesaid temperature. For its relatively slow kinetics of strengthening precipitation [140–142], this superalloy is considered to have good weldability when low heat inputs are employed, minimizing the Nb segregation and the Laves phase formation. Several works reported a strong tendency to microfissuring in HAZ, favored by the segregation of Nb and Mo in the FZ during the localized solidification process of the bead, with consequent formation of the brittle and detrimental (Ni, Cr, Fe)₂(Nb, Mo, Ti, Si) Laves phase in the interdendritic regions [62,73,116,143]. The microfissuring mechanism also depends on the characteristics of the base material. For instance, the microfissuring is mainly attributed respectively to the NbC- δ phase in wrought alloy and to the Laves phase and carbides in the cast alloy [73]. Besides this difference, Alvarez et al. [57] reported a limited effect of the material state on the weldability of wrought and cast IN718, although the grain size was respectively 30 μ m for the wrought and 1 mm for the cast, which is a significant variation. Indeed, there are works in which the effect of pre-welding heat treatments is also considered. For example, in [77,144] the base material was solution treated at 980 °C, while in [73] a comparison between three different pre-welding states is carried out: as-received, solution treated at 955 °C, and a combination of solution treatment plus aging. The authors revealed that the solution-treated samples presented a larger amount of δ phase and Niobium segregation at grain boundaries. The presence of Laves phase is also affected by the process parameters selected. According to [108], increase heat input leads to an increase in the bead dimensions and to a coarser microstructure. In this work, several process parameters were combined to optimize the welds, but the authors reported no differences in the weldability since no microfissuring was observed in none of the conditions analyzed. The grain size strongly affects the mechanical properties of the joints, and for this reason it is beneficial to reduce the heat input on the material. In addition, it was found that using oscillation laser is beneficial to decrease the grain size, reducing the thermal gradients in the bead [63].

Concerning the EBW application on this type of superalloy, different investigations focused either on the optimization of the process parameters or on the application of PWHT (post-welding heat treatment) can be found in the literature. An example in the first category is presented by Mei et al. [103], where the effect of welding speed on the microstructure and mechanical properties of EBW on Inconel 718 alloy is studied. By increasing the welding speed from 1143 to 1270 mm/min, they observe a reduction of Nb micro-segregation in the region near the center of the weld pools, hindering the Laves phase formation, and leading to a reduction of the crack susceptibility. Reddy et al. [101]

observed beneficial effects in tensile strength and ductility of IN718 weld by using an elliptical electron beam. The beam oscillation helps in reducing the thermal gradients while increasing the cooling rates: thus the G/R ratio will decrease, favoring solidification in equiaxed dendritic mode. Moreover, the segregation of Nb and the Laves phase formation are impeded. It must be mentioned that microcracks often originate from the decohesion of the interface between Laves phases and γ matrix under a tensile stress. Therefore, besides the amount of Laves phases, other factors must be taken into account, such as the size, distribution, and Nb content of the phases. Indeed, long chains of coarse Laves particles are more detrimental with respect to finer and dispersed granular Laves particles [101,108]. Post-welding heat treatments can partially dissolve the Laves phases. For example, in [116], post-welding solution treatment at 980° is suggested to improve the tensile properties, although not as much as in the parent material.

The following tables (Tables 5 and 6) collect some of the parameter combinations used in the literature to perform LBW and EBW on IN 718. As mentioned in the previous sections, weldability is a consequence of the welding parameters, but it is also affected by the base material state and microstructure. Hence a proper comprehensive comparison would take into account pre-welding and post-welding heat treatments. As for the tables for IN625, the comments reported in the last column help in categorizing the studies.

Table 5. LBW procedures and parameters for IN718, with corresponding references.

IN 718-LBW					
Ref.	Laser Types	Thickness [mm]	Laser Power [W]	Welding Speed [mm/min]	Comments
[108]	CO ₂	1.6	2900 2512 2000 1500	2336.4 1905 1193.4 711	Effect of the heat input
[63]	Fiber	3.6	3200	600	Effect of the laser oscillation
[143]	Fiber	3	1800	1400	Optimal parameters for defect-free welds
[144]	Nd-YAG pulsed	2	400	120	Effect of heat treatments
[73]	CO ₂	5	60008000	25004000	Optimal parameters for defect-free welds
[66]	Nd-YAG	2	3000–3500	3000–4500	Effect of the filler material rate
[57]	Continuous laser Pulsed laser	3.2	2300 3166 (peak)	499.8 499.8	Investigation on crack susceptibility

Table 6. EBW parameters for IN718 and corresponding references.

IN718-EBW					
Ref.	Thickness [mm]	Acc. Voltage [kV]	Current [mA]	Welding Speed [mm/min]	Comments
[106]	12	1st pass: 60 2nd pass: 60	120 30	66 66	Effect of PWHT
[101]	3.1	55 with BO: 55	22 24–25	1500 1500	Effect of beam oscillation (B.O.) patterns
[116]	2	60	20	480	Effect of PWHT
[103]	1.6	125	65	1270	Effect of pre-welding condition and welding speed

AF955 alloy is an example of the great variability of performance and characteristics that can be achieved starting from IN718. Different products are obtained by changing the chemical composition through alteration of combinations and quantities of the main chemical elements, or by altering the microstructural features by taking advantage of different heat treatments. The versatility of IN718 makes this superalloy a valid candidate for investigations where high energy density welding technologies are applied.

6.3. Nimonic 263

Nimonic 263 is a wrought Ni-based superalloy developed post-war by Rolls-Royce [145]. The chemical composition is reported in Table 7 below.

Table 7. Nominal chemical composition of Nimonic C263 (%wt).

Co	Cr	Mo	Ti	Fe	Mn	Al	Si	C	Ni
20.0	20.0	5.8	2.1	0.7	0.6	0.45	0.4	0.06	Bal.

Nimonic 263 is known for combining excellent mechanical properties such as creep resistance at elevated temperatures [12], high surface stability with excellent corrosion and oxidation resistance, as well as high machinability and excellent weldability. It is one of the most promising candidates for future generation power plants [145]; thus, it is an alloy of great interest. The alloy is strengthened by both solid solution and precipitation with a volume fraction typically around 20% of the γ' Ni₃(Ti, Al) phase with L12 crystallographic FCC-ordered structure. The main strengthening element for the solid solution of the austenitic γ matrix is Mo, having a significant difference in atomic size compared to the FCC matrix [146]. MC carbides, rich in Ti and Mo in the form of MC phases, and M₂₃C₆ carbides rich in Cr, Ni, Mo, and Co were observed to precipitate at the grain boundaries and intragranularly [146]. The phase stability of Nimonic 263 has been widely investigated: indeed the γ' phase might transform in the η phase, precipitating at the grain boundaries. The precipitation of the η phase is promoted by long-term exposure at high temperatures and strongly affects the properties of the alloy [147]. Extensive η phase precipitation in the shape of platelets was observed after prolonged exposure at 800 °C [18,147]. It is reported that at temperatures lower than 900 °C, the hexagonal η -Ni₃Ti phase also partially precipitates in the γ matrix, while for prolonged exposure times at temperatures around 750 °C, the η phase precipitates more copiously with a thin sheet morphology, significantly reducing creep resistance [18,147].

The possibility of welding Nimonic 263 components without defects is a paramount requirement to promote the adoption of this alloy in critical conditions. Conventional welding processes such as the GTA can be applied. Nonetheless, intensive thermal cycles provoke the coarsening of carbides and high residual stresses, which in turn reduces the tensile properties and creep resistance of the joints [148,149]. High energy density welding processes might be a solution to reduce these detrimental effects. However, besides this potentiality, little information is available on the use of both the LBW and the EBW process. Due to the complex microstructure and its tendency to evolve with the temperature, it might be challenging to obtain a complete welding seam on this alloy.

An example of an extensive experimental investigation on the penetration of fiber laser treatments on Nimonic 263 sheets with a thickness of 2 mm is proposed in [150], where the influence of the laser parameters is analyzed: the variation in shape and size of the dendritic structure in the MZ was evaluated, revealing a direct impact of the laser power. Moreover, the HAZ was observed to be small, which is attributed to the poor thermal conductivity of the alloy [150]. Due to the lack of information, it is difficult at present to identify optimal parameter combinations to perform LBW and EBW. This implies that this

knowledge gap must be covered with future interesting and challenging investigations on the applicability of high energy density welding processes on the Nimonic 263.

7. Conclusions

In the present work, an overview of the high energy density welding processes Laser Beam Welding (LBW) and Electron Beam Welding (EBW) was illustrated, focusing on their applications to Ni-based superalloys. In particular, the microstructure features of the FZ and HAZ of different Ni-based superalloy joints have been described, as well as the typical welding-induced defects such as secondary phases precipitation, segregations, undesired Laves phase formation, porosity, and cracks. Two different cracking mechanisms are mainly described, from which the so-called liquation and solidification cracks originate. Possible strategies to avoid the development of such defects and indications on the suitability of different superalloys for high-energy-density welding processes are given. Moreover, three polycrystalline Ni-based superalloys are presented: the solid solution strengthened Inconel 625, the precipitation age-hardened AF955 (similar to Inconel 718), and the precipitation age-hardened Nimonic 263. The latest developments on the use of LBW or EBW on those alloys are disclosed, highlighting the research gaps that must be covered to fully exploit the potentiality of the Ni-based superalloys in combination with sophisticated joining and repairing processes such as high-energy-density welding methods. Finally, it is worth highlighting that other damaging mechanisms related to environmental aspects and not covered in this review (e.g., stress corrosion cracking, oxygen absorption during welding) could occur and compromise the structural integrity of such Ni-based superalloys due to welding-induced material modifications.

Author Contributions: Writing—original draft preparation, R.D., A.V. and G.A.; Conceptualization, R.D., A.V., G.A., S.S. and A.P.; writing—review and editing, R.D., S.S., A.V., A.P., P.F. and G.A.; supervision, R.D. and P.F. All authors have read and agreed to the published version of the manuscript.

Funding: This research was funded by the Italian Ministry of University and Research, grant number PRIN 20225YNH4M “ELAPSE”, CUP C53D23001630006, PNRR.

Data Availability Statement: No new data were created or analyzed in this study. Data sharing is not applicable to this article.

Conflicts of Interest: The authors declare no conflicts of interest.

References

1. Thellaputta, G.R.; Chandra, P.S.; Rao, C.S.P. Machinability of Nickel Based Superalloys: A Review. *Mater. Today Proc.* **2017**, *4*, 3712–3721. [[CrossRef](#)]
2. Wu, Y.; Li, C.; Xia, X.; Liang, H.; Qi, Q.; Liu, Y. Precipitate coarsening and its effects on the hot deformation behavior of the recently developed γ' -strengthened superalloys. *J. Mater. Sci. Technol.* **2021**, *67*, 95–104. [[CrossRef](#)]
3. Selvaraj, S.K.; Sundaramali, G.; Dev, S.J.; Swathish, R.S.; Karthikeyan, R.; Vishaal, K.E.V.; Paramasivam, V. Recent Advancements in the Field of Ni-Based Superalloys. *Adv. Mater. Sci. Eng.* **2021**, *2021*, 9723450. [[CrossRef](#)]
4. Su, R.; Hao, D.; He, P.; Wu, D.; Wang, Q.; Dong, H.; Ma, H. Effect of Co on creep and stress rupture properties of nickel-based superalloys—A review. *J. Alloys Compd.* **2023**, *967*, 171744. [[CrossRef](#)]
5. Reed, R.C. *The Superalloys, Fundamentals and Applications*; Cambridge University Press: Cambridge, UK, 2006.
6. Cottrell, A.H.; Bilby, B.A. Dislocation theory of yielding and strain ageing of iron. *Proc. Phys. Soc. Sect. A* **1949**, *62*, 49–62. [[CrossRef](#)]
7. Goodfellow, A.J. Strengthening mechanisms in polycrystalline nickel-based superalloys. *Mater. Sci. Technol.* **2018**, *34*, 1793–1808. [[CrossRef](#)]
8. Calvo, J.; Penalva, M.; Cabrera, J.M. Characterization of Strain-Induced Precipitation in Inconel 718 Superalloy. *J. Mater. Eng. Perform.* **2016**, *25*, 3409–3417. [[CrossRef](#)]
9. Sohrabi, M.J.; Mirzadeh, H. Unexpected formation of delta (δ) phase in as-cast niobium-bearing superalloy at solution annealing temperatures. *Mater. Lett.* **2020**, *261*, 127008. [[CrossRef](#)]

10. Cao, G.; Sun, T.; Wang, C.; Li, X.; Liu, M.; Zhang, Z.; Hu, P.; Russell, A.; Schneider, R.; Gerthsen, D.; et al. Investigations of γ' γ'' and δ precipitates in heat-treated Inconel 718 alloy fabricated by selective laser melting. *Mater. Charact.* **2018**, *136*, 398–406. [[CrossRef](#)]
11. Rafiei, M.; Mirzadeh, H.; Malekan, M. Micro-mechanisms and precipitation kinetics of delta (δ) phase in Inconel 718 superalloy during aging. *J. Alloys Compd.* **2019**, *795*, 207–212. [[CrossRef](#)]
12. Maldini, M.; Angella, G.; Lupinc, V. Analysis of creep curves of a nickel base superalloy in a wide stress/temperature range. *Mater. Sci. Eng. A* **2007**, *462*, 436–440. [[CrossRef](#)]
13. Pollock, T.M.; Tin, S. Nickel-Based Superalloys for Advanced Turbine Engines Chemistry, Microstructure, and Properties. *J. Propuls. Power* **2006**, *22*, 361–374. [[CrossRef](#)]
14. Maldini, M.; Angella, G.; Lupinc, V. Meccanismi di addolcimento ed incrudimento dovuti allo sviluppo di raft in una superlega monocristallina a base di nichel. *Metall. Ital.* **2011**, *103*, 33–40.
15. Kaciulis, S.; Mezzi, A.; Amati, M.; Montanari, R.; Angella, G.; Maldini, M. Relation between the microstructure and microchemistry in Ni-based superalloy. *Surf. Interface Anal.* **2012**, *44*, 982–985. [[CrossRef](#)]
16. Huron, E.S.; Reed, R.C.; Hardy, M.C.; Mills, M.J.; Montero, R.E.; Portella, P.D.; Telesman, J. (Eds.) *Superalloys 2012*; John Wiley & Sons: Hoboken, NJ, USA, 2012.
17. Brown, E.E.; Muzyka, D.R. *The Superalloys II*; Wiley: New York, NY, USA, 1987.
18. Angella, G.; Donnini, R.; Ripamonti, D.; Maldini, M. The role of particle ripening on the creep acceleration of Nimonic 263 superalloy. *MATEC Web Conf.* **2014**, *14*, 14001. [[CrossRef](#)]
19. Andersson, J. Review of Weldability of precipitation hardening Ni- and Fe-Ni- based superalloys. In Proceedings of the 9th International Symposium Superalloy 718 & Derivatives: Energy, Aerospace, and Industrial Applications, PittsBurgh, PA, USA, 3–6 June 2018; pp. 899–916.
20. Prager, M.; Shira, C.S. Welding of Precipitation Hardening Nickel-Base Alloys. *Weld. Res. Council. Bull.* **1968**, *6*, 128–155.
21. Franklin, J.E.; Savage, W.F. Stress relaxation and strain-age cracking in Rene 41 weldments. *J. Weld. Join.* **1974**, *53*, 380–387.
22. Andersson, J. Weldability of Ni-based Superalloys. In Proceedings of the 8th International Symposium on Superalloy 718 and Derivatives, PittsBurgh, PA, USA, 28 September–1 October 2014; p. 249.
23. Vincent, R. *Precipitation Around Welds in the Nickel-Base Superalloy, Inconel 718*; Elsevier: Amsterdam, The Netherlands, 1985; Volume 33.
24. Banovic, S.; DuPont, J.; Marder, A. Dilution and microsegregation in dissimilar metal welds between super austenitic stainless steel and nickel base alloys. *Sci. Technol. Weld. Join.* **2002**, *7*, 374–383. [[CrossRef](#)]
25. Lippold, J.C.; Kiser, S.D.; DuPont, J.N. *Welding Metallurgy and Weldability of Nickel-Base Alloys*; John Wiley & Sons: Hoboken, NJ, USA, 2009.
26. Wang, H.-S.; Huang, C.-Y.; Ho, K.-S.; Deng, S.-J. Microstructure evolution of laser repair welded René 77 nickel-based superalloy cast. *Mater. Trans.* **2011**, *52*, 2197–2204. [[CrossRef](#)]
27. Zhang, X.; Chen, H.; Xu, L.; Xu, J.; Ren, X.; Chen, X. Cracking mechanism and susceptibility of laser melting deposited Inconel 738 superalloy. *Mater. Des.* **2019**, *183*, 108105. [[CrossRef](#)]
28. Egbewande, A.T.; Buckson, R.A.; Ojo, O.A. Analysis of laser beam weldability of Inconel 738 superalloy. *Mater. Charact.* **2010**, *61*, 569–574. [[CrossRef](#)]
29. Ojo, O.A.; Richards, N.L.; Chaturvedi, M.C. Microstructural study of weld fusion zone of TIG welded IN 738LC nickel-based superalloy. *Scr. Mater.* **2004**, *51*, 683–688. [[CrossRef](#)]
30. Ojo, O.A.; Richards, N.L.; Chaturvedi, M.C. Contribution of constitutional liquation of gamma prime precipitate to weld HAZ cracking of cast Inconel 738 superalloy. *Scr. Mater.* **2004**, *50*, 641–646. [[CrossRef](#)]
31. Montazeri, M.; Ghaini, F.M. The liquation cracking behavior of IN738LC superalloy during low power Nd:YAG pulsed laser welding. *Mater. Charact.* **2012**, *67*, 65–73. [[CrossRef](#)]
32. Kim, K.M.; Lee, U.; Lee, H.; Seo, S.M.; Chun, F.J. Quantifying Susceptibility to Solidification Cracking in Oscillated CM247LC Superalloy Welds via Vastrestraint Testing. *Met. Mater. Int.* **2023**, *29*, 777–794. [[CrossRef](#)]
33. Sekhar, N.C.; Reed, R.C. Power beam welding of thick section nickel base superalloys. *Sci. Technol. Weld. Join.* **2002**, *7*, 77–87. [[CrossRef](#)]
34. Haußmann, L.; Burbaum, B.; Stöhr, B.; Förner, A.; Freund, L.; Göken, M.; Neumeier, S. Crack-Free Welding of a Co-Base Superalloy with High γ' Precipitate Fraction. *Adv. Eng. Mater.* **2022**, *24*, 2200609. [[CrossRef](#)]
35. AL-Nafeay, R.H.; AL-Roubaiy, A.O.; Omidvar, H. Overview of Joining and Repairing Techniques of Ni-Based Superalloy for Industrial Gas Turbine Applications. *IOP Conf. Ser. Mater. Sci. Eng.* **2021**, *1094*, 012141. [[CrossRef](#)]
36. Henderson, M.B.; Arrell, D.; Larsson, R.; Heobel, M.; Marchant, G. Nickel based superalloy welding practices for industrial gas turbine applications. *Sci. Technol. Weld. Join.* **2004**, *9*, 13–21. [[CrossRef](#)]
37. Zhang, H.; Li, J.K.; Guan, Z.W.; Liu, Y.J.; Qi, D.K.; Wang, Q.Y. Electron beam welding of Nimonic 80A: Integrity and microstructure evaluation. *Vacuum* **2018**, *151*, 266–274. [[CrossRef](#)]

38. Vemanaboina, H.; Gundabattini, E.; Akella, S.; Rao, A.C.U.M.; Buddu, R.K.; Ferro, P.; Berto, F. Mechanical and metallurgical properties of co2 laser beam inconel 625 welded joints. *Appl. Sci.* **2021**, *11*, 7002. [[CrossRef](#)]
39. Wang, L.; Huang, Y.; Yang, D.; Li, H.; Peng, Y.; Wang, K. Multi-scale simulation of grain growth during laser beam welding of nickel-based superalloy. *J. Mater. Res. Technol.* **2020**, *9*, 15034–15044. [[CrossRef](#)]
40. She, L.; Wei, Y.; Wang, S.; Ma, J.; Ou, W. Welding parameter optimization of electron beam welded GH4169 superalloy based on orthogonal experiment and numerical simulation. *Mater. Res. Express* **2019**, *6*, 026567. [[CrossRef](#)]
41. Thejasree, P.; Manikandan, N.; Binoj, J.S.; Varaprasad, K.C.; Palanisamy, D.; Raju, R. Numerical simulation and experimental investigation on laser beam welding of Inconel 625. *Mater. Today Proc.* **2020**, *39*, 268–273. [[CrossRef](#)]
42. Tlili, I.; Baleanu, D.; Mohammad Sajadi, S.; Ghaemi, F.; Fagiry, M.A. Numerical and experimental analysis of temperature distribution and melt flow in fiber laser welding of Inconel 625. *Int. J. Adv. Manuf. Technol.* **2022**, *121*, 765–784. [[CrossRef](#)]
43. Hernando, I.; Arrizubieta, J.I.; Lamikiz, A.; Ukar, E. Numerical model for predicting bead geometry and microstructure in laser beam welding of inconel 718 sheets. *Metals* **2018**, *8*, 536. [[CrossRef](#)]
44. Dong, S.; Zhou, M.; Gao, K.; Shen, X. Polycrystal modeling and micromechanical simulation of nickel-based superalloy electron beam welded joint. *Mater. Sci. Eng. A* **2023**, *883*, 145507. [[CrossRef](#)]
45. Yue, N.; Pei, L.; Xu, P.; Jiang, Z.; Lin, T.; Zhou, L.; Liang, Y. Porosity suppression of nickel-based superalloy by modulated base temperature in laser welding and mechanism analysis. *J. Mater. Res. Technol.* **2024**, *30*, 4725–4738. [[CrossRef](#)]
46. Sun, Z.; Ion, J.C. Laser welding of dissimilar metal combinations. *J. Mater. Sci.* **1995**, *30*, 4205–4214. [[CrossRef](#)]
47. Patterson, T.; Hochanadel, J.; Sutton, S.; Panton, B.; Lippold, J. A review of high energy density beam processes for welding and additive manufacturing applications. *Weld. World* **2021**, *65*, 1235–1306. [[CrossRef](#)]
48. Węglowski, M.S.; Błacha, S.; Phillips, A. Electron beam welding—Techniques and trends—Review. *Vacuum* **2016**, *130*, 72–92. [[CrossRef](#)]
49. Zhan, X.; Yu, H.; Feng, X.; Pan, P.; Liu, Z. A comparative study on laser beam and electron beam welding of 5A06 aluminum alloy. *Mater. Res. Express* **2019**, *6*, 056563. [[CrossRef](#)]
50. Aqeel, M.; Gautam, J.P.; Shariff, S.M. Comparative study on autogenous diode laser, CO₂ laser-MIG hybrid and multi-pass TIG welding of 10-mm thick Inconel 617 superalloy. *Mater. Sci. Eng. A* **2022**, *856*, 143967. [[CrossRef](#)]
51. Sun, Z.; Kuo, M. Bridging the joint gap with wire feed laser welding. *J. Mater. Process. Technol.* **1999**, *87*, 213–222. [[CrossRef](#)]
52. Sun, Z.; Karppi, R. The application of electron beam welding for the joining of dissimilar metals: An overview. *J. Mater. Process. Technol.* **1996**, *59*, 257–267. [[CrossRef](#)]
53. Choudhury, B.; Singh, V.; Selvarajan, L.; Goel, S.; Chandrasekaran, M. Synergic investigation of microstructure, precipitation, and micro-segregation on Inconel 825 weldments: A comparative study between GTAW and EBW. *Mater. Chem. Phys.* **2024**, *318*, 129249. [[CrossRef](#)]
54. Angella, G.; Barbieri, G.; Donnini, R.; Montanari, R.; Richetta, M.; Varone, A. Electron beam welding of IN792 DS: Effects of pass speed and PWHT on microstructure and hardness. *Materials* **2017**, *10*, 1033. [[CrossRef](#)]
55. David, S.A.; Siefert, J.A.; Dupont, J.N.; Shingledecker, J.P. Weldability and weld performance of candidate nickel base superalloys for advanced ultrasupercritical fossil power plants part I: Fundamentals. *Sci. Technol. Weld. Join.* **2015**, *20*, 532–552. [[CrossRef](#)]
56. Schnell, A.; Hoebel, M.; Samuleson, J. A study of the weldability of gamma prime hardened superalloys. *Adv. Mater. Res.* **2011**, *278*, 434–439. [[CrossRef](#)]
57. Alvarez, P.; Vázquez, L.; Ruiz, N.; Rodríguez, P.; Magaña, A.; Niklas, A.; Santos, F. Comparison of hot cracking susceptibility of tig and laser beam welded alloy 718 by vareststraint testing. *Metals* **2019**, *9*, 985. [[CrossRef](#)]
58. Norouzian, M.; Amne Elahi, M.; Plapper, P. A review: Suppression of the solidification cracks in the laser welding process by controlling the grain structure and chemical compositions. *J. Adv. Join. Process* **2023**, *7*, 100139. [[CrossRef](#)]
59. Thébaud, L.; Villechaise, P.; Crozet, C.; Devaux, A.; Béchet, D.; Franchet, J.-M.; Rouffié, A.-L.; Mills, M.; Cormier, J. Is there an optimal grain size for creep resistance in Ni-based disk superalloys? *Mater. Sci. Eng. A* **2018**, *716*, 274–283. [[CrossRef](#)]
60. Zhang, C.; Wang, P.; Wen, Z.; Xu, Z.; He, P.; Yue, Z. Study on creep properties of nickel-based superalloy blades based on microstructure characteristics. *J. Alloys Compd.* **2022**, *890*, 161710. [[CrossRef](#)]
61. Shao, J.; Yu, G.; He, X.; Li, S.; Chen, R.; Zhao, Y. Grain size evolution under different cooling rate in laser additive manufacturing of superalloy. *Opt. Laser Technol.* **2019**, *119*, 105662. [[CrossRef](#)]
62. Kou, S. *Welding Metallurgy*; John Wiley & Sons: Hoboken, NJ, USA, 2003.
63. Yan, S.; Meng, Z.; Chen, B.; Tan, C.; Song, X.; Wang, G. Experimental study on the grain evolution induced by thermal characteristics during oscillation laser welding of IN718. *Mater. Lett.* **2022**, *323*, 132581. [[CrossRef](#)]
64. Keshavarz, M.K.; Turenne, S.; Bonakdar, A. Solidification behavior of inconel 713LC gas turbine blades during electron beam welding. *J. Manuf. Process* **2018**, *31*, 232–239. [[CrossRef](#)]
65. Kou, S.; Le, Y. Welding Parameters and the Grain Structure of Weld Metal—A Thermodynamic Consideration. *Metall. Trans. A Phys. Metall. Mater. Sci.* **1988**, *19A*, 1075–1082. [[CrossRef](#)]

66. Xiao, M.; Poon, C.; Wanjara, P.; Jahazi, M.; Fawaz, Z.; Krimbalis, P. Optimization of Nd:YAG-Laser Welding Process for Inconel 718 Alloy. *Mater. Sci. Forum* **2007**, *546–549*, 1305–1308. [[CrossRef](#)]
67. Krenz, D.; Egbewande, A.T.; Zhang, H.R.; Ojo, O.A. Single pass laser joining of Inconel 718 superalloy with filler. *Mater. Sci. Technol.* **2011**, *27*, 268–274. [[CrossRef](#)]
68. Sun, W.; Wang, S.; Tan, G.; Xin, J.; Hong, M.; Wu, M.; Chen, Y. Microstructure and mechanical properties of Inconel713C Ni3Al-based superalloy joint welded by electron beam feeding wire welding technology. *J. Manuf. Process* **2023**, *89*, 50–63. [[CrossRef](#)]
69. Banerjee, K.; Richards, N.L.; Chaturvedi, M.C. Effect of filler alloys on heat-affected zone cracking in preweld heat-treated IN-738 LC gas-tungsten-arc welds. *Metall. Mater. Trans. A Phys. Metall. Mater. Sci.* **2005**, *36*, 1881–1890. [[CrossRef](#)]
70. Ola, O.T.; Ojo, O.A.; Chaturvedi, M.C. Role of filler alloy composition on laser arc hybrid weldability of nickel-base IN738 superalloy. *Mater. Sci. Technol.* **2014**, *30*, 1461–1469. [[CrossRef](#)]
71. Fan, Y.; Chen, Z.; Zhang, C.H.; Liu, A.M. A comparison of microstructure and mechanical properties of welded thin Ti6Al4V with three different types of laser. *Mater. Res. Innov.* **2015**, *19*, S187–S192. [[CrossRef](#)]
72. Ren, W.; Lu, F.; Yang, R.; Liu, X.; Li, Z.; Elmi Hosseini, S.R. A comparative study on fiber laser and CO₂ laser welding of Inconel 617. *Mater. Des.* **2015**, *76*, 207–214. [[CrossRef](#)]
73. Hong, J.K.; Park, J.H.; Park, N.K.; Eom, I.S.; Kim, M.B.; Kang, C.Y. Microstructures and mechanical properties of Inconel 718 welds by CO₂ laser welding. *J. Mater. Process. Technol.* **2008**, *201*, 515–520. [[CrossRef](#)]
74. Saurabh, S.K.; Chand, P.; Yadav, U.S. Study of the effect of laser beam welding on joint of Nimonic 80A superalloy: An experimental approach. *Int. J. Adv. Manuf. Technol.* **2024**, *133*, 5501–5513. [[CrossRef](#)]
75. das Nevesa, M.D.M.; Lottob, A.; Berrettac, J.R.; de Rossid, W.; Júniord, N.D.V. Microstructure development in Nd:YAG laser welding of AISI 304 and Inconel 600. *Weld. Int.* **2010**, *24*, 104–113. [[CrossRef](#)]
76. Tuissi, A.; Besseghini, S.; Ranucci, T.; Squatrito, F.; Pozzi, M. Effect of Nd-YAG laser welding on the functional properties of the Ni-49.6at.%Ti. *Mater. Sci. Eng. A* **1999**, *273–275*, 813–817. [[CrossRef](#)]
77. Gobbi, S.; Zhang, L.; Norris, J.; Richter, K.H.; Loreau, J.H. High powder CO₂ and Nd-YAG laser welding of wrought Inconel 718. *J. Mater. Process. Technol.* **1996**, *56*, 333–345. [[CrossRef](#)]
78. Pang, M.; Yu, G.; Wang, H.H.; Zheng, C.Y. Microstructure study of laser welding cast nickel-based superalloy K418. *J. Mater. Process. Technol.* **2008**, *207*, 271–275. [[CrossRef](#)]
79. Kuo, T.Y.; Lin, H.C. Effects of pulse level of Nd-YAG laser on tensile properties and formability of laser weldments in automotive aluminum alloys. *Mater. Sci. Eng. A* **2006**, *416*, 281–289. [[CrossRef](#)]
80. Barbieri, G.; Cognini, F.; de Crescenzo, C.; Fava, A.; Moncada, M.; Montanari, R.; Richetta, M.; Varone, A. Process Optimization in Laser Welding of IN792 DS Superalloy. *Metals* **2024**, *14*, 124. [[CrossRef](#)]
81. Moradi, M.; Ghoreishi, M. Influences of laser welding parameters on the geometric profile of Ni-base superalloy Rene 80 weld-bead. *Int. J. Adv. Manuf. Technol.* **2011**, *55*, 205–215. [[CrossRef](#)]
82. Saurabh, S.K.; Chand, P.; Yadav, U.S. Multi-objective optimization and fracture analysis of laser weld joints of Ni-Cr superalloy 80 A for gas turbine components. *J. Mech. Sci. Technol.* **2024**, *38*, 4867–4876. [[CrossRef](#)]
83. Pakniat, M.; Ghaini, F.M.; Torkamany, M.J. Hot cracking in laser welding of Hastelloy X with pulsed Nd: YAG and continuous wave fiber lasers. *Mater. Des.* **2016**, *106*, 177–183. [[CrossRef](#)]
84. Jiang, Z.; Tao, W.; Yu, K.; Tan, C.; Chen, Y.; Li, L.; Li, Z. Comparative study on fiber laser welding of GH3535 superalloy in continuous and pulsed waves. *Mater. Des.* **2016**, *110*, 728–739. [[CrossRef](#)]
85. Gandy, D.W.; Frederick, G.; Stover, J.T.; Viswanathan, R. Overview of hot section components repair methods. In *ASM Materials Solutions Conference & Exposition, Energy & Utilities Program*; ASM International: St. Louis, MO, USA, 2000.
86. Zhu, Z.; Ma, X.; Mi, G.; Wang, C. Electron microscopy study of laser welded GH909 superalloy joint. *J. Mater. Res. Technol.* **2020**, *9*, 15525–15536. [[CrossRef](#)]
87. Yan, F.; Hu, C.; Zhang, X.; Cai, Y.; Wang, C.; Wang, J.; Hu, X. Influence of heat input on HAZ liquation cracking in laser welded GH909 alloy. *Opt. Laser Technol.* **2017**, *92*, 44–51. [[CrossRef](#)]
88. Ojo, O.A. Intergranular liquation cracking in heat affected zone of a welded nickel based superalloy in as cast condition. *Mater. Sci. Technol.* **2007**, *23*, 1149–1155. [[CrossRef](#)]
89. Osoba, L.O.; Ding, R.G.; Ojo, O.A. Microstructural analysis of laser weld fusion zone in Haynes 282 superalloy. *Mater. Charact.* **2012**, *65*, 93–99. [[CrossRef](#)]
90. Palanivel, R.; Dinaharan, I.; Laubscher, R.F.; Alarifi, I.M. Effect of Nd:YAG laser welding on microstructure and mechanical properties of Incoloy alloy 800. *Opt. Laser Technol.* **2021**, *140*, 107039. [[CrossRef](#)]
91. Wang, N.; Mokadem, S.; Rappaz, M.; Kurz, W. Solidification cracking of superalloy single- and bi-crystals. *Acta Mater.* **2004**, *52*, 3173–3182. [[CrossRef](#)]
92. Rong, P.; Wang, N.; Wang, L.; Yang, R.N.; Yao, W.J. The influence of grain boundary angle on the hot cracking of single crystal superalloy DD6. *J. Alloys Compd.* **2016**, *676*, 181–186. [[CrossRef](#)]

93. Babu, S.S.; David, S.A.; Park, J.W.; Vitek, J.M. Joining of nickel base superalloy single crystals. *Sci. Technol. Weld. Join.* **2004**, *9*, 1–12. [[CrossRef](#)]
94. Vitek, J.M.; Babu, S.S.; Park, J.W.; David, S.A. Analysis of stray grain formation in single-crystal nickel-based superalloy welds. In Proceedings of the International Symposium on Superalloys, Champion, PA, USA, 19–23 September 2004; pp. 459–465. [[CrossRef](#)]
95. Wang, Y.L.; Ojo, O.A.; Ding, R.G.; Chaturvedi, M.C. Weld metal cracking in laser beam welded single crystal nickel base superalloys. *Mater. Sci. Technol.* **2009**, *25*, 68–75. [[CrossRef](#)]
96. Churchman, C.; Bonifaz, E.A.; Richards, N.L. Comparison of single crystal Ni based superalloy repair by gas tungsten arc and electron beam processes. *Mater. Sci. Technol.* **2011**, *27*, 811–817. [[CrossRef](#)]
97. Ferro, P.; Zambon, A.; Bonollo, F. Investigation of electron-beam welding in wrought Inconel 706—Experimental and numerical analysis. *Mater. Sci. Eng. A* **2005**, *392*, 94–105. [[CrossRef](#)]
98. Siddharth, P.N.; Narayanan, C.S. A review on Electron Beam Welding process. *J. Phys. Conf. Ser.* **2020**, *1706*, 012208. [[CrossRef](#)]
99. Richards, N.L.; Nakkalil, R.; Chaturvedi, M.C. The influence of electron-beam welding parameters on heat-affected-zone microfissuring in INCOLOY 903. *Metall. Mater. Trans. A* **1994**, *25*, 1733–1745. [[CrossRef](#)]
100. Choudhury, B.; Chandrasekaran, M. Microstructural Investigation and Integrated Optimization of Weld Bead Characteristics in Electron Beam Welding of Inconel 825. *Trans. Indian. Inst. Met.* **2021**, *74*, 2681–2701. [[CrossRef](#)]
101. Madhusudhana Reddy, G.; Srinivasa Murthy, C.V.; Srinivasa Rao, K.; Prasad Rao, K. Improvement of mechanical properties of Inconel 718 electron beam welds—influence of welding techniques and postweld heat treatment. *Int. J. Adv. Manuf. Technol.* **2009**, *43*, 671–680. [[CrossRef](#)]
102. Sun, W.; Wang, S.; Hong, M.; Xin, J.; Chen, Y.; Zhang, Z.; Chen, Y. Effect of heat input on microstructure and mechanical properties of IC10 Ni3Al-based superalloy electron beam welding joint. *Vacuum* **2020**, *182*, 109765. [[CrossRef](#)]
103. Mei, Y.; Liu, Y.; Liu, C.; Li, C.; Yu, L.; Guo, Q.; Li, H. Effect of base metal and welding speed on fusion zone microstructure and HAZ hot-cracking of electron-beam welded Inconel 718. *Mater. Des.* **2016**, *89*, 964–977. [[CrossRef](#)]
104. Chen, G.Q.; Zhang, B.G.; Lü, T.M.; Feng, J.C. Causes and control of welding cracks in electron-beam-welded superalloy GH4169 joints. *Trans. Nonferr. Met. Soc. China (Engl. Ed.)* **2013**, *23*, 1971–1976. [[CrossRef](#)]
105. Arulmurugan, B.; Agilan, M.; Jerome, S.; Arivarasu, M.; Manikandan, M.; Srikanth, A.; Arivazhagan, N. Investigation of metallurgical and mechanical properties of 21st century nickel-based superalloy 686 by electron beam welding technique. *Sadhana—Acad. Proc. Eng. Sci.* **2018**, *43*, 117. [[CrossRef](#)]
106. Gao, P.; Zhang, K.F.; Zhang, B.G.; Jiang, S.S.; Zhang, B.W. Microstructures and high temperature mechanical properties of electron beam welded Inconel 718 superalloy thick plate. *Trans. Nonferr. Met. Soc. China (Engl. Ed.)* **2011**, *21*, s315–s322. [[CrossRef](#)]
107. Sun, W.; Wang, S.; Xin, J.; Chen, Y.; Pang, Y.; Jia, Y. Optimizing for IC10 single crystal Ni3Al-based alloy joint by electron beam welding with chemical composition controlling. *Mater. Des.* **2020**, *196*, 109172. [[CrossRef](#)]
108. Odabaşı, A.; Ünlü, N.; Göller, G.; Eruslu, M.N. A study on laser beam welding (LBW) technique: Effect of heat input on the microstructural evolution of superalloy inconel 718. *Metall. Mater. Trans. A Phys. Metall. Mater. Sci.* **2010**, *41*, 2357–2365. [[CrossRef](#)]
109. Taheri, M. Analysis of Solidification and Liquation Cracks in the Electron Beam Welding of IN738 Superalloy. *Metallogr. Microstruct. Anal.* **2021**, *10*, 815–822. [[CrossRef](#)]
110. Han, K.; Wang, H.; Shen, L.; Zhang, B. Analysis of cracks in the electron beam welded joint of K465 nickel-base superalloy. *Vacuum* **2018**, *157*, 21–30. [[CrossRef](#)]
111. Vishwakarma, K.R.; Richards, N.L.; Chaturvedi, M.C. Microstructural analysis of fusion and heat affected zones in electron beam welded ALLVAC® 718PLUS™ superalloy. *Mater. Sci. Eng. A* **2008**, *480*, 517–528. [[CrossRef](#)]
112. Taheri, M.; Kashani-Bozorg, S.F.; Alizadeh, A.; Beni, M.H.; Jam, J.E.; Khorram, A. Analysis of liquation and solidification cracks in the electron beam welding of GTD-111 nickel-base superalloy joint. *Mater. Res. Express* **2021**, *8*, 076507. [[CrossRef](#)]
113. Ojo, O.A.; Wang, Y.L.; Chaturvedi, M.C. Heat affected zone liquation cracking in electron beam welded third generation nickel base superalloys. *Mater. Sci. Eng. A* **2008**, *476*, 217–223. [[CrossRef](#)]
114. Sun, W.; Xin, J.; Wang, S.; Chen, Y.; Huang, Y. Effect of deposited layer thickness on the microstructure and mechanical properties of IC10 single-crystal Ni3Al-based alloy electron beam-welded joint. *J. Mater. Res. Technol.* **2021**, *11*, 1206–1219. [[CrossRef](#)]
115. Haines, M.; Plotkowski, A.; Frederick, C.L.; Schwalbach, E.J.; Babu, S.S. A sensitivity analysis of the columnar-to-equiaxed transition for Ni-based superalloys in electron beam additive manufacturing. *Comput. Mater. Sci.* **2018**, *155*, 340–349. [[CrossRef](#)]
116. Janaki Ram, G.D.; Venugopal Reddy, A.; Prasad Rao, K.; Madhusudhan Reddy, G. Microstructure and mechanical properties of Inconel 718 electron beam welds. *Mater. Sci. Technol.* **2005**, *21*, 1132–1138. [[CrossRef](#)]
117. Chen, G.L. *Theory of Superalloy*; Metallurgy Industry Press: Beijing, China, 1988.
118. Danis, Y.; Arvieu, C.; Lacoste, E.; Larrouy, T.; Quenisset, J.M. An investigation on thermal, metallurgical and mechanical states in weld cracking of Inconel 738LC superalloy. *Mater. Des.* **2010**, *31*, 402–416. [[CrossRef](#)]
119. Wen, S.; Liu, Z.; Mi, D.; Li, B.; Yang, S.; Jiang, C. Revealing the fatigue crack propagation mechanism of a Ni-based superalloy electron beam welded joint through in-situ SEM observation. *Int. J. Fatigue* **2022**, *162*, 106955. [[CrossRef](#)]

120. Special Metals Corporation Products. INCONEL® Alloy 625 (technical bulletins). Available online: www.specialmetals.com/products (accessed on 10 December 2024).
121. Quist, W.E.; Taggart, R.; Polonis, D.H. The influence of iron and aluminum on the precipitation of metastable Ni₃Nb phases in the Ni-Nb system. *Metall. Trans.* **1971**, *2*, 825–832. [[CrossRef](#)]
122. Sundararaman, M.; Mukhopadhyay, P.; Banerjee, S. Precipitation of the δ -Ni₃Nb phase in two nickel base superalloys. *Metall. Trans. A* **1988**, *19*, 453–465. [[CrossRef](#)]
123. Kohl, H.; Peng, K. Thermal stability of the superalloys Inconel 625 and Nimonic 86. *J. Nucl. Mater.* **1981**, *101*, 243–250. [[CrossRef](#)]
124. Sundararaman, M.; Mukhopadhyay, P. Heterogeneous Precipitation of the γ'' Phase in Inconel 625. *Mater. Sci. Forum* **1985**, *3*, 273–280. [[CrossRef](#)]
125. Floreen, S.; Fuchs, G.E.; Yang, W.J. The Metallurgy of Alloy 625. In Proceedings of the Superalloys 718, 625, 706 and Various Derivatives, Pittsburgh, PA, USA, 27–29 June 1994; pp. 13–38.
126. Muzyka, D.R. *The Superalloys*; John Wiley & Sons: New York, NY, USA, 1972.
127. Shankar, V.; Bhanu Sankara Rao, K.; Mannan, S.L. Microstructure and mechanical properties of Inconel 625 superalloy. *J. Nucl. Mater.* **2001**, *288*, 222–232. [[CrossRef](#)]
128. Charles, T.; Tait, P. The performance of alloy 625 in long-term intermediate temperature applications. *Int. J. Press. Vessel. Pip.* **1994**, *59*, 41–49.
129. Shoemaker, L.E. Alloys 625 and 725: Trends properties and applications. In Proceedings of the Superalloys 718, 625, 706 and Various Derivatives, Pittsburgh, PA, USA, 2–5 October 2005; pp. 409–418.
130. Gessinger, G.H.; Bomford, M. Powder metallurgy of superalloys. *Int. Metall. Rev.* **1974**, *19*, 51–76. [[CrossRef](#)]
131. Jelokhani-Niaraki, M.R.; Arab, N.B.M.; Naffakh-Moosavy, H.; Ghoreishi, M. The systematic parameter optimization in the Nd:YAG laser beam welding of Inconel 625. *Int. J. Adv. Manuf. Technol.* **2016**, *84*, 2537–2546. [[CrossRef](#)]
132. Caiazzo, F.; Alfieri, V.; Cardaropoli, F.; Sergi, V. Investigation on edge joints of Inconel 625 sheets processed with laser welding. *Opt. Laser Technol.* **2017**, *93*, 180–186. [[CrossRef](#)]
133. Hong, M.; Wang, S.; Sun, W.; Geng, Z.; Xin, J.; Ke, L. Effect of welding speed on microstructure and mechanical properties of selective laser melting Inconel 625 alloy laser welded joint. *J. Mater. Res. Technol.* **2022**, *19*, 2093–2103. [[CrossRef](#)]
134. Ramkumar, K.D.; Mulimani, S.S.; Ankit, K.; Kothari, A.; Ganguly, S. Effect of grain boundary precipitation on the mechanical integrity of EBW joints of Inconel 625. *Mater. Sci. Eng. A* **2021**, *808*, 140926. [[CrossRef](#)]
135. Romanin, L.; Ferro, P.; Bonollo, F.; Berto, F. A numerical and experimental analysis of Inconel 625 electron-beam welding—Thermal aspects. *Procedia Struct. Integr.* **2019**, *18*, 63–74. [[CrossRef](#)]
136. Li, J.; Yao, J.; Zhao, G.; Li, H.; Li, Y.; Liu, J. The Influence of Different Focusing Currents on the Microstructure Evolution and Wear Properties of a Scanning Electron Beam Modified Inconel 625 Nickel Base Alloy Surface. *Crystals* **2023**, *13*, 325. [[CrossRef](#)]
137. Shakil, M.; Ahmad, M.; Tariq, N.H.; Hasan, B.A.; Akhter, J.I.; Ahmed, E.; Mehmood, M.A.; Choudhry, M.A.; Iqbal, M. Microstructure hardness studies of electron beam welded Inconel, 6.2.5.; stainless steel, 3.0.4.L. *Vacuum* **2014**, *110*, 121–126. [[CrossRef](#)]
138. Ramkumar, K.D.; Sridhar, R.; Periwal, S.; Oza, S.; Saxena, V.; Hidad, P.; Arivazhagan, N. Investigations on the structure—Property relationships of electron beam welded Inconel 625 and UNS 32205. *Mater. Des.* **2015**, *68*, 158–166. [[CrossRef](#)]
139. Wiednig, C.; Lochbichler, C.; Enzinger, N.; Beal, C.; Sommitsch, C. Dissimilar electron beam welding of nickel base alloy 625 and 9% Cr steel. *Procedia Eng.* **2014**, *86*, 184–194. [[CrossRef](#)]
140. Qi, H.; Azer, M.; Ritter, A. Studies of standard heat treatment effects on microstructure and mechanical properties of laser net shape manufactured INCONEL 718. *Metall. Mater. Trans. A Phys. Metall. Mater. Sci.* **2009**, *40*, 2410–2422. [[CrossRef](#)]
141. Zhong, C.; Gasser, A.; Kittel, J.; Wissenbach, K.; Poprawe, R. Improvement of material performance of Inconel 718 formed by high deposition-rate laser metal deposition. *Mater. Des.* **2016**, *98*, 128–134. [[CrossRef](#)]
142. Çam, G.; Koçak, M. Progress in joining of advanced materials. *Int. Mater. Rev.* **1998**, *43*, 1–44. [[CrossRef](#)]
143. Sharma, S.K.; Biswas, K.; Nath, A.K.; Manna, I.; Dutta Majumdar, J. Microstructural change during laser welding of Inconel 718. *Optik* **2020**, *218*, 165029. [[CrossRef](#)]
144. Janaki Ram, G.D.; Venugopal Reddy, A.; Prasad Rao, K.; Reddy, G.M.; Sarin Sundar, J.K. Microstructure and tensile properties of Inconel 718 pulsed Nd-YAG laser welds. *J. Mater. Process. Technol.* **2005**, *167*, 73–82. [[CrossRef](#)]
145. Smith, S.A.; West, G.; Chi, K.; Gamble, W.; Thomson, R. Microstructural Evolution in Nimonic 263 for High Temperature Power Plant. In *Advances in Materials Technology for Power Plants, Proceedings from the 6th International Conference, Santa Fe, NM, USA, 31 August–3 September 2010*; ASM International: Materials Park, OH, USA, 2015; pp. 110–126.
146. Zhao, J.C.; Ravikumar, V.; Beltran, A.M. Phase precipitation and phase stability in Nimonic 263. *Metall. Mater. Trans. A Phys. Metall. Mater. Sci.* **2001**, *32*, 1271–1282. [[CrossRef](#)]
147. Detrois, M.; Jablonski, P.D.; Hawk, J.A. The effect of η phase precipitates on the creep behavior of alloy 263 and variants. *Mater. Sci. Eng. A* **2021**, *799*, 140337. [[CrossRef](#)]
148. Jeon, M.; Lee, J.H.; Woo, T.K.; Kim, S. Effect of welding and post-weld heat treatment on tensile properties of Nimonic 263 at room and elevated temperatures. *Metall. Mater. Trans. A Phys.* **2011**, *42*, 974–985. [[CrossRef](#)]

149. Li, Y.; Fan, X.; Cui, H.; Lu, F.; Tang, X. The correlated mechanism of creep fracture and microstructure evolution for precipitated Nimonic 263 superalloy welding joint. *Sci. Technol. Weld. Join.* **2020**, *26*, 37–46. [[CrossRef](#)]
150. Sharma, A.K.; Anand, M.; Kumar, V.; Kumar, S.; Das, A.K. Laser Beam Treatment of Nimonic C263 Alloy: Study of Mechanical and Metallurgical Properties. In *Advances in Micro and Nano Manufacturing and Surface Engineering; Lecture Notes on Multidisciplinary Industrial Engineering*; Shunmugam, M., Kanthababu, M., Eds.; Springer: Singapore, 2019; pp. 633–646. [[CrossRef](#)]

Disclaimer/Publisher’s Note: The statements, opinions and data contained in all publications are solely those of the individual author(s) and contributor(s) and not of MDPI and/or the editor(s). MDPI and/or the editor(s) disclaim responsibility for any injury to people or property resulting from any ideas, methods, instructions or products referred to in the content.